Optical remote sensing and change detection for landslide mapping in a humid climate

Julie Risti Bergaas

Thesis submitted as part of the degree in Master of Science
Master in Geomorphology and Geomatics
60 credits

Department of Geoscience
Faculty of Mathematics and Natural Sciences

UNIVERSITY OF OSLO

June 2021

Optical remote sensing and change detection for landslide mapping in a humid climate

Supervisor: Dr. Andreas Max Kääb[1]
Co-supervisor: Dr. James Michael Strout[2]

1. Department of Geoscience, University of Oslo, Oslo, Norway
2. Norwegian Geotechnical Institute, Oslo, Norway

http://www.duo.uio.no/

Printed: Reprosentralen, University of Oslo

Abstract

Previous landslides can be important indicators for where to expect future landslide activity and under which conditions. Unfortunately, information concerning previous landslides is often insufficient and landslide databases are incomplete. Only a subset of landslides is registered, in most cases those who interact or affect human life and infrastructure. However, landslides often appear in remote areas, and several landslides, therefore, remain unknown and unnoticed.

This study proposes the use of free accessible optical satellite data, produced by moderate resolution sensors in combination with vegetation indices to map and detect previous landslides. The focus is change detection analysis using images from the Sentinel 2 and Landsat 8 optical satellites, which are post-processed to calculate various vegetation indices. Primarily two vegetation indices are used, Atmospherically Resistant Vegetation Index (ARVI) and Normalized Difference Vegetation Index (NDVI). The mapping of landslides is performed in ArcMap, where two different mapping approaches are undertaken. First, a manual mapping where the difference between pre-and post-image is studied. Secondly, a semi-automatic mapping approach in the Raster Calculator. These mapping approaches are applied to Jølster municipality for detecting landslides after the Jølster landslide event in 2019.

After the event, 18 landslides were defined within Jølster municipality and registered in the NVEs landslide database. In this study, a total of 108 landslides were identified. A comparative analysis in ArcMap, between ARVI and NDVI, reveals that ARVI detected changes caused by landslides better than NDVI. To verify the method, it has been applied to a second study site; Oso located in the state of Washington, USA. At this case site as well, ARVI maps more accurately than NDVI for landslide recognition.

This study suggests that moderate resolution, optical satellite images used in the study of detecting previous landslides increases the number of detected landslides. Further, the vegetation index ARVI should be used when detecting landslides in humid climates. Throughout the research conducted, this study contributes to an improved understanding of the Jølster event, as well as a comparison of different methods for remote landslide detection. The research contributes supplementary landslide information to the database of already known landslides. Furthermore, testing and comparison of methods contribute towards an understanding of best-practice.

Acknowledgments

I would like to thank my supervisors Andreas Max Kääb and James Michael Strout for the opportunity, technical supervision, and great guidance. This last year has been incredibly educational. Thank you for introducing me to different approaches using remote sensing data in combination with vegetation indices, for mapping and detecting landslides.

This work is directly linked to the SFI Klima2050, the studies of Ph.D. candidate Erin Lindsay (NTNU), and ongoing research activities at NGI. In this context, I would like to thank Erin Lindsay for allowing me insight into her study, in addition to Dr. Regula Frauenfelder and Dr. Sean Salazar (both from NGI) who contributed with technical support and advice. In addition, I would like to thank Dr. Graziella Devoli (NVE) for giving me an introduction to how the existing landslide database in Norway is structured.

For this master thesis, Geodata AS has given me a free educational software license in ArcGIS Pro, needed for my work. I would like to thank Rebecca Bakke working at Geodata, for technical support.

At last, I would like to thank fellow students, friends, and family. Thank you for cheering me on through this last year. Especially, I would like to thank Edvardt Saugen who has shown a great interest in my work, even if it is out of your educational background. Thank you for supporting me, and especially for making sure dinner is ready after late nights at the University.

Table of Contents

Abstract iii
Acknowledgments v
Table of Contents vii
List of Figures ix
List of Tables x
Acronyms and Abbreviation xi
1 Introduction 1
1.1 Motivation and Aim 1
1.2 Research Needs 1
1.3 Objectives 1
1.4 Background 2
1.5 Outline 3
2 Landslide hazards 5
2.1 Increase in Landslide hazards 5
2.2 Landslide Classification 7
2.3 Historical data inventories need improvement 8
2.4 Remote sensing as a landslide analysis tool 10
3 Theoretical Background 12
3.1 Overview: Remote sensing 12
3.2 Data sets – availability and limitations 14
3.3 Change detection algorithms 18
4 Study areas and previous work 20
4.1 Jølster, Norway 20
4.2 Oso, Washington 23
5 Method 27
5.1 Data collection 27
5.2 Software 28
5.3 Analytical approach 28
5.3.1 Manual Landslide Mapping 31

5.3.2 Landslide mapping in Raster Calculator 33
6 Results 36
6.1 Vegetation indices - Jølster 36
6.1.1 ARVI and NDVI differences calculated with Sentinel 2 36
6.1.2 ARVI and NDVI differences calculated with Landsat 8 37
6.2 Landslides and other elements of interest 39
6.3 Vegetation Indices - Oso 42
6.4 Additional Vegetation Indices 44
6.5 Landslide detection – Manual Mapping 45
6.6 Landslide detection in Raster Calculator 50
7 Discussion 52
7.1 Data collection and visualization 52
7.1.1 Study areas 52
7.1.2 Data collection and pre-processing 53
7.1.3 Vegetation indices and Water indices 55
7.2 Landslide Mapping 58
7.2.1 Manual mapping 58
7.2.2 Landslide mapping in Raster calculator 60
7.3 Comparison to previous work by Lindsay (2021) 63
7.4 Implications of this study 63
8 Conclusions 65
8.1 Main findings 65
8.2 Weaknesses 66
8.3 Recommendations for further work 66
9 References 68

List of Figures

Figure 1: Statistics of how many days' landslide warnings were given in Norway from 2013 until 2020. 5
Figure 2: The map contains landslide warnings caused by precipitation and heavy rain in Norway from 2013 until 2021.. 6
Figure 3: The updated version of Varnes classification system by Hungr et al. (2014). 7
Figure 4: Overview of the orbital configuration of Sentinel 2. 12
Figure 5: Overview of both the Landsat 8 and the Sentinel 2 satellite and their instruments.. 13
Figure 6: Band combination of Landsat 7, Landsat 8, and Sentinel 2. 16
Figure 7: Overview of the main project area, Jølster municipality in Norway. 20
Figure 8: Soil- and slope map over Jølster municipality. 21
Figure 9: Overview of the second project area, Oso located in Washington, USA. 23
Figure 10: Slope cross-section showing the stratigraphy of the terrace northeast of Oso. 24
Figure 11: Overview of the workflow for calculating NDVI and dNDVI. 31
Figure 12: Calculation of dARVI with Sentinel 2A L1- and Sentinel 2A L2 data. 36
Figure 13: Calculation of dNDVI with Sentinel 2A L1 - and Sentinel 2A L2 data. 37
Figure 14: Displays dARVI calculated with Landsat 8 data. 38
Figure 15: Displays dNDVI calculated with Landsat 8 data. 38
Figure 16: An enlarged section of Jølster municipality is shown in A, B, C, and D, displayed with dARVI and dNDVI calculated with Sentinel 2 data. 39
Figure 17: Displays dARVI and dNDVI calculated with Landsat 8 data for an enlarged section of Jølster municipality. 40
Figure 18: dARVI and dNDVI calculated with Landsat 8 data displayed over the cloud-affected area in Sentinel 2A. 41
Figure 19: Displays dARVI calculated with Sentinel 2A L2, Sentinel 2A L1, and Landsat 8 L1. 42
Figure 20: Calculation of dARVI with Landsat 8 data over the Oso study area in Washington 43
Figure 21: Calculation of dNDVI with Landsat 8 data over the Oso study area in Washington. 43
Figure 22: Overview of all the indices calculated in this study with the use of Sentinel 2 L2 data. 45
Figure 23: Landslides mapped manually using dARVI. 46
Figure 24: Display of both landslides manual mapped with Sentinel 2 data and Landsat 8 data 49
Figure 25: Displays landslides mapped with the use of both Sentinel 2 and Landsat 8, in addition the location of landslides in NVEs existing landslide database. 50
Figure 26: The results from the landslide mapping in the Raster Calculator using Equation 1 51
Figure 27: The result from the landslide mapping in the Raster Calculator using Equation 2. 51

List of Tables

Table 1: Sentinel 2 band combination. Information reconstructed from (ESA, n.d.-d). 15
Table 2: Landsat 8 band combination. Information reconstructed from USGS (n.d.-a). 15
Table 3: Overview of the places affected by natural hazards 30. July 2019, in Vestland County. Table modified from NVE (2019). 22
Table 4: Values from both dARVI and dNDVI within the landslide polygon drawn around the landslide in Oso in 2014. 44
Table 5: Statistics derived from Zonal Statistics of the 20 cases where dNDVI was better than dARVI to map landslides in Jølster, with the use of Sentinel 2A as post-image. 47
Table 6: Statistics derived from Zonal Statistics of the 11 cases where dNDVI was better than dARVI to map landslides in Jølster, with the use of Sentinel 2B as post-image. 47
Table 7: Statistics derived from Zonal Statistics of the 20 best cases where dARVI was better than dNDVI to map landslides in Jølster, with the use of Sentinel 2A as post-image. 48
Table 8: Statistics derived from Zonal Statistics of the 11 best cases where dARVI was better than dNDVI to map landslides in Jølster, with the use of Sentinel 2B as post-image. 48

Acronyms and Abbreviation

ARVI	Atmospherically Resistant Vegetation Index
DTM	Digital Terrain Model
EO	Earth Observation
EVI	Enhanced Vegetation Index
EWS	Early Warning System
GIS	Geographic Information System
GNDVI	Green Normalized Vegetation Index
InSAR	Interferometric synthetic aperture radar
L1	Level 1
L2	Level 2
L8	Landsat 8
LiDAR	Light Detecting and Ranging
LSWI	Land Surface Water Index
MSI	Multispectral Imager
NDVI	Normalized Difference Vegetation Index
NDWI	Normalized Difference Water Index
NIR	Near Infra-Red
OLI	Operational Land Imager
RS	Remote Sensing
S2	Sentinel 2
SWIR	Short Wave Infra-Red
TIRS	Thermal Infra-Red sensor

1 Introduction

1.1 Motivation and Aim

Landslides are growing problems. The risk associated is accelerating due to climate change, growing populations, and land-use change (Zhong et al., 2020). Landslides occur globally, in different climate conditions and terrains, complicating the effort of predicting accurately when and where landslides will occur (Highland & Bobrowsky, 2008; Zhong et al., 2020). The diversity of triggering mechanisms causes a broad area of potential landslide exposure, and the severity of the damage is often unpredictable. This especially regards fast-moving landslide types such as debris flows. This type of landslide is one of the most destructive and often no warnings are available in advance. Based on the abovementioned, it is difficult to prepare for such events and warning mitigation also struggles with fast-moving landslides (Highland & Bobrowsky, 2008).

Previous landslides can be a good indicator of where to expect landslide activity in the future (Shahabi et al., 2013), and landslides are often proven to be repetitive (Malamud et al., 2004). The work of mapping areas already affected by landslides is therefore crucial for the understanding of where to expect landslide activity in the future. This study aims to develop a user-friendly approach to identify landslides in a cost-effective way.

1.2 Research Needs

Historical data about previous landslides are limited and improvement of landslide statistical databases is needed (Mondini et al., 2019; Van Westen et al., 2008). This master thesis suggests that this improvement can be done using free accessible, optical satellite images, in combination with Geographical Information Systems (GIS). Further, undertake a change detection where the goal is to identify-rainfall induced landslides by interpreting different vegetation indices. To test this, the approach will be applied to two test sites.

1.3 Objectives

The objectives of this study are to test the efficacy of change detection analysis using optical satellite images that are post-processed to calculate various vegetation indices. The underlying hypothesis is thereby that landslides destroy vegetation and become thus detectable through vegetation loss. Variables to be assessed are image sources providing various resolutions, and

the vegetation indices Atmospherically Resistant Vegetation Index (ARVI) and Normalized Difference Vegetation Index (NDVI). The comparative analysis is to be carried out in a GIS framework. Moreover, the study will specifically focus on evaluating the applicability of satellite data produced by moderate resolution sensors and a simplified GIS workflow to provide landslide detection over large areas and regions.

Sentinel 2 and Landsat 8 data are chosen as data sources to study the use of free accessible satellite data, and whether the moderate resolution is good enough for landslide detecting after a heavy-rainfall event. Further, vegetation indices are widely used in the study of detecting changes. NDVI is the most commonly used vegetation index (Bannari et al., 1995). Both study areas introduced in this thesis have a humid climate that is highly affected by clouds, air humidity, and high precipitation amounts, which often influence the satellite images, and can potentially invalidate the result (SafeLand D4.5, 2011). ARVI corrects NDVI for atmospheric effects (Kaufman & Tanre, 1992), and is therefore calculated to study if the resistance of the index to such effects can improve the results in humid regions.

Finally, to summarize the four research questions to be addressed are:

- Can optical satellite data be used to identify landslides and expand landslide inventories after heavy-rainfall events, and is this a recommended approach?
- Is moderate resolution good enough for detecting and recognize landslides?
- Does landslide size and location affect the quality of the method?
- Through a subset of six known indices, which index is most appropriate to use for identifying previous landslides?

1.4 Background

This subject is directly connected to Klima 2050 which "is a Centre for Research-based Innovation (SFI)". The aim of Klima 2050 is to "reduce the societal risk associated with climate changes" (Klima 2050, n.d.). The Jølster landslide event in 2019 has been a focus, and detecting landslides from this specific event is the main focus in this thesis.

The work of Ph.D. Candidate Erin Lindsay is especially important. As part of her Ph.D. study, Lindsay contributes to collecting landslide data from Jølster after the event 30th of July 2019, with the use of remote sensing images. In similarity to this master thesis, she utilizes the free accessible Sentinel 2 data, in addition to the vegetation indices NDVI for detecting landslides. bases her method of calculating the change between images from before and after the event,

and assumes a change in land surface cover from vegetation to bare soil, utilizing the vegetation index NDVI.

Lindsay (2021) uses both Sentinel 1 and Sentinel 2 data, for utilizing both optical and radar data. Her results show that Sentinel 1 is negatively affected by topography, and of 120 landslides detected with Sentinel 2, only 3 were easily detectable with Sentinel 1, 6 were detectible given prior knowledge and 111 was not detectable. Further, she collected data with higher resolution than Sentinel 2 and argue that other optical sources with higher resolution have limited potential for improved detail mapping. However, she concludes that other types of data may still be useful like data collected by drones which can give better information about where the landslide initiated.

If possible, the results of this thesis will be compared to the results obtained in the Ph.D. study of Lindsay (2021). A comparative analysis between NDVI and ARVI will be accounted for.

1.5 Outline

This master thesis is organized as follows:

Chapter 1 (this section) presents a general introduction containing research objectives and background, defining the content of the thesis.

Chapter 2 presents a general introduction to landslide hazard as a problem, including the principal application area. Hereunder key problems like climate, population, and collection of historical landslide information are described.

Chapter 3 provides the theoretical background needed for the study, divided into an overview of remote sensing, opportunities and limitations of using moderate-resolution optical satellite data, and change detection algorithms.

Chapter 4 introduces the two project areas, Jølster and Oso, in addition to previous work done at these case sites.

Chapter 5 describes the method used in this study, presenting data collection, software used, and analytical approaches.

Chapter 6 presents the results obtained from the method, categorized by type of data used, different approaches, and location.

Chapter 7 contains the discussion of the results and approaches, in addition to a comparison between results from different studies.

Chapter 8 presents the conclusions, framed in the context of the research questions. Faults, errors, and weaknesses in the study are presented in addition to recommended further research.

Chapter 9 presents the references used in this thesis, listing the background theory for this work.

2 Landslide hazards

2.1 Increase in Landslide hazards

Every year, landslides impact both the built environment and the natural environment. They may cause damage to buildings, transport routes, economic disruption, and take human lives. The wildlife on land, in lakes, and at sea may also be affected (Highland & Bobrowsky, 2008). In Norway, several landslides get triggered every year. In 2019, twenty-eight events regarding floods and landslides were documented (NVE, 2020a), and respectively in 2020, nineteen events were documented (NVE, 2021). Both years, the landslides caused human death and damage to infrastructure. In Norway, landslide warnings are categorized in different levels represented by colors. This classification is based on the probability of occurrence and the extent of damage and danger to the population. There are a total of four danger levels: Green level indicates safe conditions, a yellow level representing a challenging situation where local damage may occur, orange level representing a serious situation where serious damage can occur, and last, red level indicates an extreme situation which can cause severe damage (NVE, n.d.). During the last years, there has been an increasing trend in the frequency of landslide warnings. In 2019, landslide warnings were given on 49 days, 44 at a yellow level and five at an orange level. In 2020, 66 days had landslide warnings, 64 with yellow level and two with orange level (NVE, 2020a, 2021). Figure 1 shows statistics of how many days' landslide warnings were alerted in the period between 2013 and 2020. Warnings regarding heavy precipitation are given from 2016 until 2020. Before 2016, warnings of heavy precipitation were given by the Norwegian Meteorological Institute (MET), separately (Devoli, Colleuille, et al., 2020).

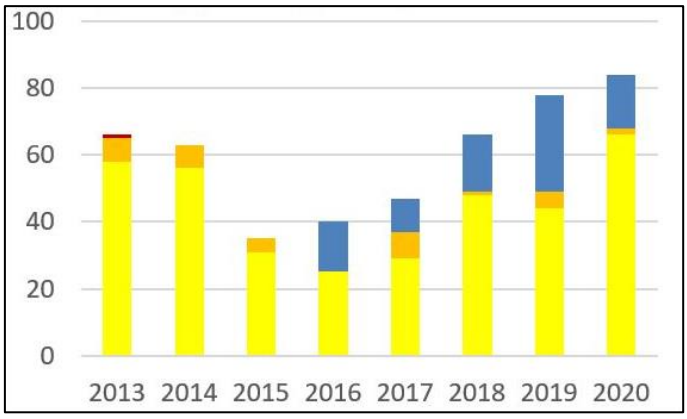

Figure 1: Statistics of how many days' landslide warnings were given in Norway from 2013 until 2020. The numbers of landslide warning are indicated with the colors yellow, orange and red, based on their danger level, and further, days of heavy precipitation is indicated with a blue color. During the last five years, the trend of warnings has increased. Figure from NVE (2021).

In the future, researchers expect the frequency of landslides will increase due to change in climate conditions (Agersten et al., 2019). The Intergovernmental Panel on Climate Change (IPCC) has shown that over the last 150 years the temperature on Earth's surface has risen (Smith, 2013). According to the Norwegian Meteorological Institute (MET), the average temperature in 2020 was the highest recorded average temperature in 120 years, indicating an increasing trend (NVE, 2021). In addition, values at most meteorological measuring stations in Norway reports that during the past 50 years the highest daily precipitation has increased, and there is a positive trend for frequency and intensity of heavy rain lasting from 10 to 60 minutes. Due to this, we can expect more variations in climate conditions during the year, and consequently, these fluctuations and rapid changes in weather conditions can potentially cause severe damage (Agersten et al., 2019).

At the end of July 2019, Jølster municipality, located in the western part of Norway, experienced such an increase in heavy precipitation. The precipitation was more intense than initially expected and caused the trigger of several landslides. Consequences of the landslides included destruction of buildings, destruction of roads, and one human death. Even though warnings were sent out, they were underestimated, according to MET (Agersten et al., 2019). This event is referred to as the Jølster event. Figure 2 shows that especially the western part of Norway has a high number of landslide warnings when precipitation and heavy rain are the cause.

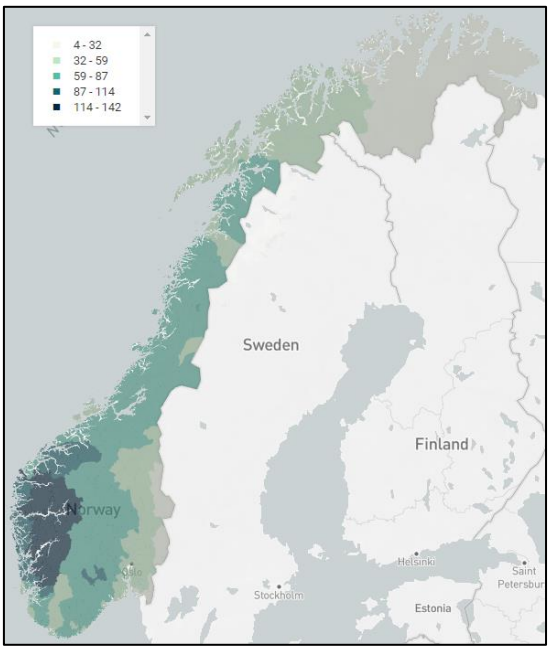

Figure 2: The map contains landslide warnings caused by precipitation and heavy rain in Norway from 2013 until 2021. The map indicates an especially high number of landslide warnings in the western part of Norway. Source: DSB (n.d.).

2.2 Landslide Classification

A landslide can be defined as a mass moving down-slope under the force of gravity. Size and velocity vary, depending on the topography and which types of material the landslide consists of. It can consist of various types of surface material and is classified according to this (Smith, 2013). There are several ways to categorize different types of landslides, looking at e.g. material composition, water content, movement, velocity, and volume (Hungr et al., 2001). The landslide classification system by Varnes is well-developed and widely used by scientists. In a new version, the classification proposes 32 types of landslides which are categorized by type of movement and type of material, distinguishing between rock and soil (Figure 3) (Hungr et al., 2014). In Norway, landslides are categorized into three groups by type of material, rock, soil, and snow (NGU, 2014; NVE, 2020c).

Type of movement	Rock	Soil
Fall	1. *Rock/ice* fall[a]	2. *Boulder/debris/silt* fall[a]
Topple	3. Rock block topple[a]	5. *Gravel/sand/silt* topple[a]
	4. Rock flexural topple	
Slide	6. Rock rotational slide	11. *Clay/silt* rotational slide
	7. Rock planar slide[a]	12. *Clay/silt* planar slide
	8. Rock wedge slide[a]	13. *Gravel/sand/debris* slide[a]
	9. Rock compound slide	14. *Clay/silt* compound slide
	10. Rock irregular slide[a]	
Spread	15. Rock slope spread	16. *Sand/silt* liquefaction spread[a]
		17. Sensitive clay spread[a]
Flow	18. *Rock/ice* avalanche[a]	19. *Sand/silt/debris* dry flow
		20. *Sand/silt/debris* flowslide[a]
		21. Sensitive clay flowslide[a]
		22. Debris flow[a]
		23. Mud flow[a]
		24. Debris flood
		25. Debris avalanche[a]
		26. Earthflow
		27. Peat flow
Slope deformation	28. Mountain slope deformation	30. Soil slope deformation
	29. Rock slope deformation	31. Soil creep
		32. Solifluction

Figure 3: The updated version of Varnes classification system by Hungr et al. (2014). The table contains 32 different natural hazards divided into types of movement, rock, and soil.

The most common triggering factors for landslides are natural processes like heavy rain, rapid snowmelt, earthquakes, and in some cases, human activity (Smith, 2013; Zhong et al., 2020). Triggering mechanisms varies for different types of landslides, e.g. heavy precipitation and rapid snowmelt are common triggering mechanisms for debris flow and slides in general. These factors often lead to saturation of slope, in addition to an increase in groundwater level within the mass. Intense surface water may also erode soil or rock which can lead to failure (Highland

& Bobrowsky, 2008). The gradient of the slope is an important factor for where different types of landslides initiate and how they spread downhill. For instance, debris flow usually gets triggered in channels where the slope gradient is between 25 and 45 degrees (NVE, 2020b). Rockfalls, on the other hand, get triggered more commonly by weathering processes like frost-thaw activity or intense vibration, and the slope gradient is usually above 45 degrees (Dorren, 2003). Rock fall can also be a triggering mechanism to other landslides such as debris flow if the rocks cause disturbance in saturated soil (NVE, 2020b).

However, natural processes are by far the only reason why landslides get triggered. Human activity plays a large role in the occurrence of many landslides, etc. excavation and undercutting of slopes during building processes or maintenance in addition to loading on top of the slope, changing of the drainage system and leaking pipes, in addition to removal of vegetation (Highland & Bobrowsky, 2008). Moreover, the combination of human activity and climate change can also potentially cause instability and failure.

As the human population grows, there will be a need to inhabit areas that are uninhabited today. In Norway, regulations for land-use change are strict, and in areas where new real estate development is planned, regulations on technical requirements, as well as risk assessments, apply. These regulations intend to maintain safety and prevent new buildings from being negatively impacted regarding stability and safety in the future. These regulations take geographic differences and climate conditions into account, but a future change in climate and adoption yields great uncertainty (DSB, 2015; Plan- og bygningsloven, 2015). For instance, slope stability can change in the future due to changes in climate conditions. As a result of this, areas that previously were considered sufficiently safe for development, no longer meet the requirements for safety in the Planning and Building Act and other building regulations (DSB, 2015).

2.3 Historical data inventories need improvement

Historical landslide inventories provide useful information about the spatial distribution of landslides from the past (Shahabi et al., 2013). Landslide inventories can be categorized based on what information the map represents, e.g., inventories that represent landslides after one specific event or inventories representing one type of mass movement. Typical information to find in landslide inventories is; location, date, size, type of mass movement, triggering factors and in some cases additional information like deposits and erosion features (Guzzetti et al., 2012).

Much of the research regarding landslide mapping and detection is based on the well-known saying; “The past and present are keys to the future” (Carrara et al., 1991; Varnes, 1984). The importance of this saying can be recognized in landslide inventory mapping being of great importance in landslide hazard and risk assessment (Behling et al., 2014), in addition, it is the first step in the risk identification process (Andersson-Sköld et al., 2013). Moreover, the observed landslides in inventory maps are of great importance for creating susceptibility models and are used as input for validating and calibrating them (Chang et al., 2007; Guzzetti et al., 2006; Rossi et al., 2010). These maps are ordinary based on historical information of past landslides, analysis of aerial photographs and field investigations (Guzzetti et al., 2012; Malamud et al., 2004; Soeters & Van Westen, 1996). The different approaches vary for different inventory types and the map scales (Guzzetti et al., 2012).

There are still many regions in the world where inventories do not exist and those that do are limited. The quality and accuracy of the inventory map depend on the completeness, and consequently, the databases used represent only a subset of landslides: those that are registered and recorded (Guzzetti et al., 2012). Much of the previously recorded data is based on statistical approaches, either quantitative or qualitative, but where everything relying on known landslides (Cruden, 2018). This is predominantly underestimated for unpopulated areas and where human structures such as roads and railways are lacking (Carrara et al., 2003). However, landslides often appear in landscapes where it is difficult or impossible for humans to inspect from the ground. Many landslides, therefore, remain unknown and unnoticed, unless they interact or affect human life (Mondini et al., 2019).

Moreover, the temporal update rate for inventories is a source of error as it is often limited to several years (Behling et al., 2016). Every year, several landslides trigger and cause damage to buildings and the natural environment (Highland & Bobrowsky, 2008), and without a continuous update of inventory maps, important information is lost and predictions for future landslides get less precise and reliable.

Inventory- and susceptibility maps are important elements in Early Warning Systems (EWS) in Norway. Norwegian Water Resources and Energy Directorate (NVE) has the main responsibility of landslide detection in Norway which began in 2013. For many of the registered landslides in the national landslide database, important information is missing. Several of the issues, including spatial bias and missing information like the number of incidents, size, and triggering factors, remaining for EWS, could be solved with better landslide inventories (Devoli, Jarsve, et al., 2020). Moreover, no single organization has the overall responsibility

for landslide registration in remote areas. Consequently, landslides occurring in remote areas are reported randomly and in heterogeneous format. The ad-hoc reports and the heterogeneous nature of the reports limit the overall accuracy for landslide inventories (Lindsay, 2017). New methods for systematic change detection should be introduced to address this problem.

2.4 Remote sensing as a landslide analysis tool

In recent years, different remote sensing (RS) techniques are developing rapidly (SafeLand D4.1, 2012). RS enables detection and monitoring of large areas from distance, and remote detection of landslide exposure is a great advantage since many landslides are triggered in inaccessible, remote areas (Hölbling et al., 2015). Remote sensors measure reflected and emitted radiation and are typically installed on satellites or aircraft (USGS, n.d.-d). Both spaceborne and airborne RS methods play an important role in gathering information concerning environmental phenomena (SafeLand D4.5, 2011), such as geology and geomorphology, land cover use, and landscape changes, all important to understand and observe landslide activity (Zhong et al., 2020). Satellites cover a wider area than aerial photographs and the revisiting time can be up to a few days. The revisiting time for aerial photography is more limited and irregular (A. Mondini et al., 2011). Ongoing missions have proven that almost every spaceborne and airborne technique gathers reliable information for detecting and mapping (SafeLand D4.5, 2011).

There are two primary types of RS instruments, passive and active. Passive sensors detect and measure reflected or emitted radiation. The instruments are weather-dependent and rely on illumination from the sun. Active sensors, on the other hand, measure reflected or backscattered radiation from signals transmitted from the sensor. For instance, radar and SAR can collect data in all weather conditions both day and night. The contribution of both instrument types, passive and active, has proven to be a powerful method in landslide mapping and detection in addition to hazard analysis (SafeLand D4.5, 2011).

Further, the most common data used for post-failure mapping is optical RS data retrieved from passive sensors (Behling et al., 2014). Modern optical satellites record and provide images with a high temporal and spatial resolution (SafeLand D4.5, 2011). These images are convenient for monitoring changes in the landscape, including changes caused by landslide activity (Rau et al., 2007). Some of the images, depending on which satellite it is collected, are available for free download which simplifies the collection of relevant data. Each image is signed with a date, which gives an approximate date to previous events by comparing satellite images before

and after, looking for changes. By comparing pre- and post-imagines a relationship between geomorphological conditions and land cover changes, before and after an event, can be established (Shahabi & Hashim, 2015). This bi-temporal approach is widely used for post-failure mapping (Cheng et al., 2004; Lacroix et al., 2013).

The information collected from optical satellite images is important for understanding when to expect high frequency for landslides during the year and by comparing the date with meteorological data, triggering factors can be discovered. The availability of high- and very-high resolution satellite images is increasing and contributing to research into and development of automatic and semi-automatic methods for mapping and detect landslides (Guzzetti et al., 2012). With an increase in diversity, it has been observed that there also is an increase in the effectiveness and reliability of RS techniques related to mapping and detecting landslides (SafeLand D4.5, 2011).

Preliminary studies using RS data on the Jølster events indicate that this area is promising as a test case for mapping and detection of recent landslides (Lindsay, 2017). After the event of 30th July 2019, 13 landslides in Vestland county in Norway were documented at Varsom, which is a platform for landslide warnings. By looking at RS data, traces of several other landslides appear, especially in remote areas.

3 Theoretical Background

3.1 Overview: Remote sensing

Remote sensing has a long tradition, going back to 1858, when images were taken from a balloon over Paris, France (Blaschke et al., 2014). RS images taken from aircraft were first used in the 1920s for geological purposes and became a common approach in the 1930s (Watson, 1994). Approximately 40 years later, spaceborne RS came on the market due to the launch of Landsat-1 in 1972 (Blaschke et al., 2014). Over the years, satellite images have increasingly replaced aerial photographs in the study of landslide mapping and detection (A. Mondini et al., 2011).

The majority of earth observation satellites in orbit carry passive sensors such as Sentinel 2 and Landsat 8 (SafeLand D4.1, 2012). The Sentinel 2 constellation consists of two identical satellites where Sentinel 2A was launched in 2015 and Sentinel 2B was launched in 2017. These satellites are 180 degrees apart in node longitude, in the same sun-synchronous 786 km orbit. They provide optimal coverage of all land surfaces on Earth, with a revisiting time of 5 days (10 days for one). Sentinel 2 carries a multispectral imager (MSI) which provides a wide swath width of 290 km and a large band set of 13 multispectral bands in the visible and Near Infra-Red (NIR) spectrum (ESA, n.d.-e). Their mission and aim are to provide data continuity to the Landsat, SPOT, and ASTER missions, among others (Van der Meer et al., 2014). Figure 4 shows the Sentinel 2 orbital configuration.

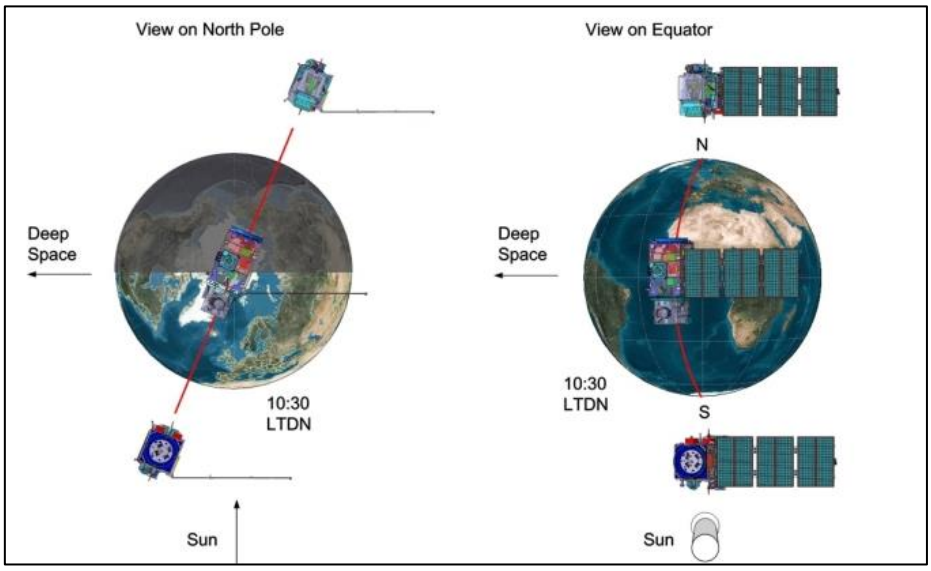

Figure 4: Overview of the orbital configuration of Sentinel 2. To the left, the configuration is shown from the view on the North Pole, and to the right, the view on the Equator. Figure from ESA (n.d.-c).

Landsat 8 was developed by the National Aeronautics and Space Administration (NASA) and U.S. Geological Survey (USGS) and launched in 2013. Landsat 8 consists of two instruments, the Operational Land Imager (OLI) and the Thermal Infrared Sensor (TIRS), which provide global coverage of the earth's surface (NASA, n.d.). It has an altitude of 705 km in a sun-synchronous, near-polar orbit, with a swath width of 185 km. The revisit time is 16 days. Landsat 8 is improved in many ways compared to previous Landsat sensors. The radiometric resolution is better and the number of images taken each day has significantly increased due to an improved duty cycle (Roy et al., 2014). OLI provides two new spectral bands for observing costal aerosols (Band 1) and detect cirrus clouds (Band 9). TIRS also provides two new spectral bands in the thermal region. These bands were for previous Landsat sensors covered by one wider band. Altogether, Landsat 8 provides 11 bands, both multispectral and thermal, in addition to panchromatic bands (NASA, n.d.).

Both Sentinel 2 and Landsat 8 have a medium resolution compared to other high- and very high-resolution satellites like Quickbird and Ikonos (Deilami & Hashim, 2011). Figure 5 shows Landsat 8 and Sentinel 2 and their instruments.

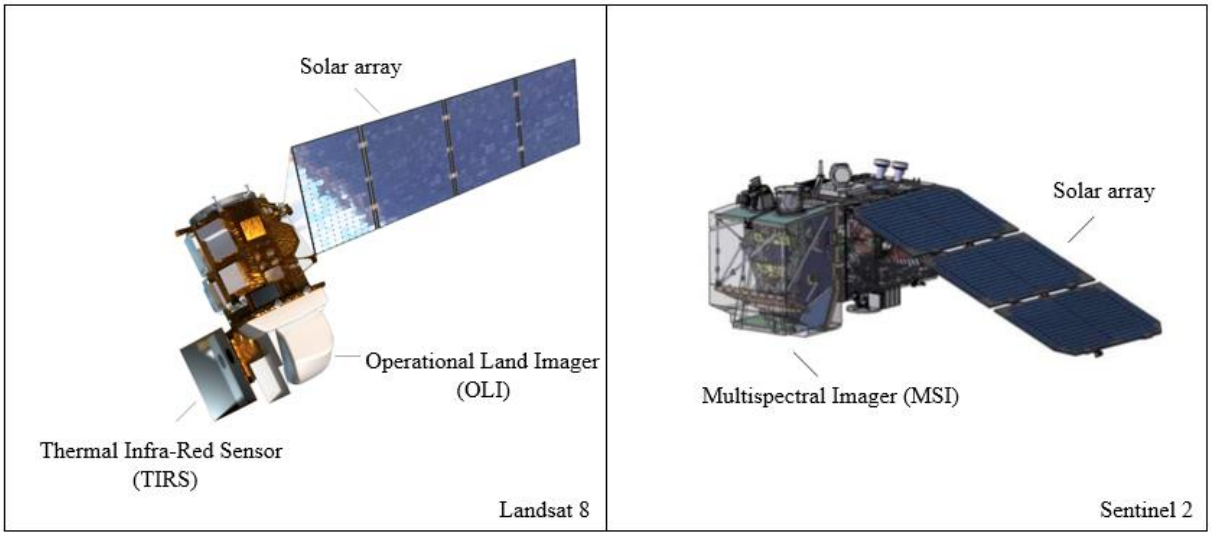

Figure 5: Overview of both the Landsat 8 and the Sentinel 2 satellite and their instruments. The figure of Landsat 8 is collected from NASA (n.d.) and the figure of Sentinel 2 is from ESA (2015).

Until now, few studies have used different optical datasets and compared the mapping results. More studies comparing and evaluating uncertainties among landslide inventories developed from the results from different sensors are needed (SafeLand D4.5, 2011).

Guzzetti et al. (2012) and Li et al. (2016), classify previous methods in landslide mapping using optical RS images in two groups; pixel-based and object-based. Usually, the smallest entity in an RS image is a pixel (Blaschke et al., 2004), while an object is a group of pixels where the pixels have similar values (Hay et al., 2001). The pixel-based method is rather simple to apply and gives the best results in areas where surface changes predominantly are caused by landslide activity. In situations, where other factors such as deforestation cause changes, the accuracy is limited (SafeLand D4.5, 2011). The method is sensitive to noise and if the spectral information is limited, it may fail (Lu et al., 2019).

Since 1972, the majority of methods developed for image processing are pixel-based (Blaschke et al., 2014), but since around the year 2000, this approach has been criticized (Burnett & Blaschke, 2003; Fisher, 1997). The first commercial software for analyzing objects in RS images was then developed (Blaschke et al., 2014), to widen the investigation of contextual and spatial features of landslides (Martha et al., 2010; Martha et al., 2012). The object-based approach is usually applied when using very high-resolution satellite images (Blaschke et al., 2014), and can in principal achieve better accuracy than the pixel-based (Lu et al., 2019). By using an object-based approach, clustering pixels to objects of varying sizes can give meaningful and detailed information about the characteristics in the different image objects and has a great potential for accurate landslide change detection. These characteristics can further be used in semi-automatic landslide detection and mapping (Hölbling et al., 2015). A limitation to the object-based approach is that it can be more general compared to pixel-based methods. It is important to provide appropriate criteria's when using an object-based approach, which may be more time-consuming, and expertise is often needed (Mondini et al., 2011).

3.2 Data sets – availability and limitations

Compared to other satellites with free access, Sentinel 2 has the great advantage of 10-meter resolution in 4 bands; red, green, blue, and near-infrared (NIR) (Lacroix et al., 2018; Yang et al., 2019). The remaining bands have a resolution of 20- and 60-meter. Landsat 8, which also is free accessible provides a spatial resolution of 30-meter for visible, NIR, and SWIR, 100 meters for the thermal bands, and 15-meter for the panchromatic band (NASA, n.d.). An overview of the bands provided from Sentinel 2 and Landsat 8 can be found in table 1 and table 2. Overall, the spectral bands of Sentinel 2 and Landsat 8 are very similar, except Landsat 8 provides thermal bands (Figure 6) (USGS, n.d.-c). The difference between level 1 (L1) and level 2 (L2) is similar for Sentinel 2 and Landsat 8 (USGS, n.d.-b). Level-1 data is radiometric and geometric corrected, in addition, includes spatial registration and orthorectification (ESA,

n.d.-a). Where else, Level-2 data includes atmospheric corrections and a scene classification (ESA, n.d.-b).

Table 1: Sentinel 2 band combination. Information reconstructed from (ESA, n.d.-d).

Sentinel 2			
Bands	Central wavelength (nm)	Bandwidth (nm)	Resolution (m)
Band 1 - Coastal aerosol	442.7	21	60
Band 2 - Blue	492.4	66	10
Band 3 - Green	559.8	36	10
Band 4 - Red	664.6	31	10
Band 5 - Vegetation Red Edge	704.1	15	20
Band 6 - Vegetation Red Edge	740.5	15	20
Band 7 - Vegetation Red Edge	782.8	20	20
Band 8 - Near Infra-Red (NIR)	832.8	106	10
Band 8A - Vegetation Red Edge	864.7	21	20
Band 9 - Water Vapour	945.1	20	60
Band 10 - Short Wave Infra-Red (SWIR) -Cirrus	1373.5	31	60
Band 11 - SWIR	1613.7	91	20
Band 12 - SWIR	2202.4	175	20

Table 2: Landsat 8 band combination. Information reconstructed fromUSGS (n.d.-a).

Landsat 8			
Bands	Central wavelength (nm)	Bandwidth (nm)	Resolution (m)
Band 1 - Coastal aerosol	440	20	30
Band 2 - Blue	480	60	30
Band 3 - Green	560	60	30
Band 4 - Red	655	30	30
Band 5 - Near Infra-Red (NIR)	865	30	30
Band 6 - Shorth Wave Infra-Red (SWIR) 1	1610	80	30
Band 7 - SWIR 2	2200	180	30
Band 8 - Panchromatic	590	180	15
Band 9 - Cirrus	1370	20	30
Band 10 - Thermal Infra-Red (TIRS) 1	10895	590	100
Band 11 - Thermal Infra-Red (TIRS) 2	12005	1010	100

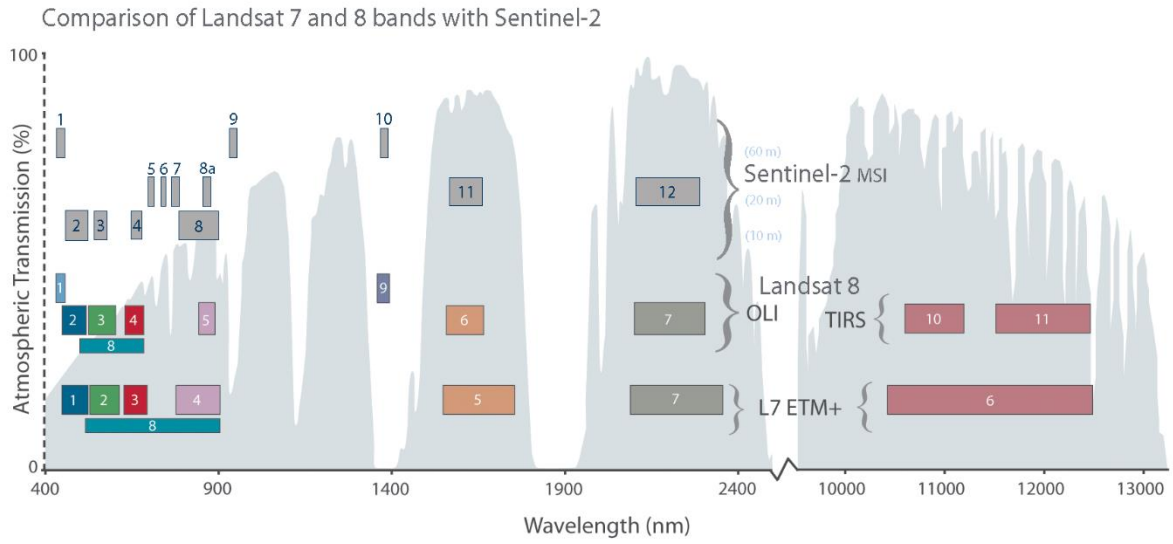

Figure 6: Band combination of Landsat 7, Landsat 8, and Sentinel 2. Table from USGS (n.d.-c).

The medium resolution of both Landsat 8 and Sentinel 2, makes it hard to detect smaller landslides. Landsat is preferred for regional coverage, typically thousands of square kilometers and problems regarding mapping landslides occur if the landslide is less than a few hundred square meters (SafeLand D4.4, 2011). Earlier attempts explain that landslide mapping with Landsat suffers from coarse resolution (SafeLand D4.1, 2012). For Sentinel 2, landslides smaller than 10x10 cannot be captured. Difficulties also occur when detecting only a few centimeters of slope displacement with 10-meter spatial resolution, compared with Synthetic Aperture Radar (SAR) techniques. However, Sentinel 2 is appropriate for detecting fast-moving ground motions, like debris flow (Yang et al., 2019). Overall, spaceborne techniques provide a wide area coverage and thereby usually coarser spatial resolution and poorer accuracy level (SafeLand D4.4, 2011). Therefore, many studies still rely on aerial photographs with higher resolution (SafeLand D4.1, 2012).

Change in vegetation is often used as an indicator of landslide activity using optical satellite images. Optical RS methods can therefore be an important supplement to methods using SAR technology, especially in vegetated areas. Vegetation signals are often seen as noise using SAR techniques, which limit the method, especially over areas with a high percentage of dense vegetation (Yang et al., 2019). However, changes in vegetation can also cause trouble for optical RS techniques. The spectral, spatial, and temporal characteristics of a landslide are not unique and landslides can be covered by other land covers. Moreover, the landslide surface material and features are affected by many factors including geological, geomorphological, and hydrological ones which can vary greatly, in addition to weather conditions (Zhong et al., 2020).

Over the years, landslide masses will change, especially due to revegetation and erosion, and the signs of them will decrease. Temporal resolution is in this case very important and when to collect post-event images has to be taken into consideration (Behling et al., 2016). Limitations for accurate detecting and mapping of landslides also occur where the area of interest both contains fresh and old landslides (Hölbling et al., 2015). Several regions experience recurring landslides (Malamud et al., 2004), and if an area contains landslide material, a new landslide will not necessarily make a distinguished change that can be caught by the satellite sensor. This cluster of landslides can result in landslides being connected to the wrong event, in addition to not separating the landslides correctly, which can reduce the accuracy of the correct number of landslides after an event (Hölbling et al., 2015).

In the study of change detection, the perfect scenario is collecting images with no cloud cover. However, this is almost impossible as the globe is covered by close to 70% of clouds (Altaweel, 2017). Clouds and cloud shadows in optical satellite images will affect the results of change detection analysis. They distort the signal captured by the satellite sensor and corrupt the images (Mill et al., 2014). Based on this, it is crucial to remove all pixels representing clouds to detect the true surface change and get reliable results (Mill et al., 2014; Yang et al., 2019). Removal of clouds is therefore one of the first steps in data processing of optical RS images (Gómez-Chova et al., 2017). The algorithm used to remove clouds depends on which spectral bands are available (Hagolle et al., 2010). For instance, clouds are typically colder than the earth's surface and thermal IR bands can be used to detect this (Ackerman et al., 1998; Hunt, 1973; Saunders & Kriebel, 1988). The blue band is of good use for detecting low clouds if the surface is not too bright like snow-covered (Bréon & Colzy, 1999). Further, snow and clouds can look similar in optical RS images. SWIR bands can distinguish between snow and clouds because the reflectance range between these targets is greater in SWIR than for Visible and NIR (Dozier, 1989).

There are several approaches to remove clouds and shadows from optical satellite images. One method is to replace the areas that are covered by clouds, with a cloud-free image, by clipping the area. With this approach, seasonal variation among other things, that can differentiate the two overlapping images, is a problem (Altaweel, 2017). The cloud-free image taking on another date may also not show the changes of interest. Moreover, pixel sorting where multiple images that are not too dark or bright are used, due to shadows and clouds, is a more common approach. With rapid computation and machine learning, the images can seamlessly be merged. Images from different sensors can also be used, which is a great advantage (Sharma et al., 2017).

Google Earth is used similarly today (Altaweel, 2017). Automated cloud detection is another alternative. Here, pixels representing clouds in the optical satellite image can be masked and removed from the dataset. Clouds are identified by looking at variance in reflectance, using time series data, where a rapid change in reflectance is interpreted as clouds. These areas can again be merged with no-cloud cover images. Multi-Temporal Cloud Detection is a method that looks for an increase in reflectance in the blue wavelengths, and an abrupt increase can be automatically identified as clouds, using linear correlation (Hagolle et al., 2010). Further, cloud masking or data to merge and remove the clouds can be added (Altaweel, 2017).

3.3 Change detection algorithms

Vegetation indices are of good use in the interpretation process of satellite images and contribute as a useful method for land cover change detection. Several vegetation indices have been developed for both qualitatively and quantitatively evaluating the vegetation cover. Calculations of vegetation indices are a processing technique that combines the various frequency bands embedded in an image to produce a composite image where certain characteristics are highlighted or suppressed in the images. For example, a vegetation index would cause typical vegetative features in the image to appear more strongly (brighter) than non-vegetative features (Bannari et al., 1995).

Compared to individual spectral bands, the use of vegetation indices results in a better sensitivity for green vegetation (Bannari et al., 1995). Research has shown that especially the spectral response of the red and NIR channels are good for this study. The red band correlates with chlorophyll concentration and the NIR band is controlled by the density of green vegetation in addition to leaf area index (Major et al., 1990).

Change detection is done by comparing images taken at different times to identify features that appear, disappear or move over time. By applying the combination of indices and change detection, features of interest can first be highlighted which will improve the subsequent change detection calculation. Once the data is in a GIS framework, various raster calculations and subsequent change detection analyses can be easily made on those data sets.

Hundreds of vegetation indices are developed for different purposes, but the perfect vegetation index does not exist (Major et al., 1990). Several factors can affect vegetation indices, both biological and physical. Researchers have therefore tried to combine different channels in many ways to eliminate these disturbance factors (Bannari et al., 1995).

Normalized Difference Vegetation Index (NDVI) is a commonly used by-product for optical images collected by satellites and is used for identifying landslides in the form of surface changes (Yang et al., 2017; Zhang et al., 2018). The results are often better in tropical and equatorial areas where landslide activity causes distinct land cover changes due to the great presence of dense vegetation (Guzzetti et al., 2012). The formula of NDVI utilizes the red and NIR band, proven to be useful in the study of landslide change detection (Major et al., 1990). As previously mentioned, shadow-affected areas can be a problem in mapping and detecting landslides using optical satellite images. Fiorucci et al. (2019) argue that the use of this vegetation index can lessen the impact of shadow, and confirms that the use of NDVI improves the result of mapping and visual recognize landslides in shadow-affected areas. Until now, only a few studies have tried combining NDVI with Sentinel 2 data to examine the NDVI potential to identify and recognize landslide change processes (Qu et al., 2021). NDVI is still the most used vegetation index and is often used as a reference, evaluating new other indices (Bannari et al., 1995). In this thesis, NDVI will be used to evaluate the vegetation index ARVI.

Atmospheric effects in addition to absorption and scattering cause difficulties for interpreting changes at the Earth's surface using optical RS images. Especially the Red- and NIR bands are influenced by these variations (Kaufman, 1988; Slater, 1980). Based on this, Kaufman and Tanre (1992) developed the Atmospherically Resistant Vegetation Index (ARVI), an index that is self-corrected for atmospheric effects. Originally, ARVI was developed to be used by the MODIS sensor, but can also be used for other sensors (Kaufman & Tanre, 1992). A new combination, a red-blue channel, given by the difference in radiation between the two, can reduce atmospheric scattering effects in the red channel (Bannari et al., 1995). The improvements that ARVI contributes, work better for vegetated areas compared to soil, it also works better for small aerosols particles than for larger (Kaufman & Tanre, 1992). ARVI can be seen as a new redefinition version of NDVI, and the dynamic range is similar (Bannari et al., 1995). This vegetation index uses the same bands as NDVI, in addition to the blue band. Moreover, ARVI is still responsive to changes in green vegetation, and in addition, resistant to atmospheric effects. To achieve this, the focus is on reducing the atmospheric effect on the red band. This is because the red band is more sensitive to atmospheric effects than NIR. However, the fact that NDVI is normalized reduces several factors including atmospheric effects. Still, by comparing the two indices, ARVI is four times less sensitive than NDVI to atmospheric effects (Kaufman & Tanre, 1992).

4 Study areas and previous work

4.1 Jølster, Norway

The main study area is Jølster municipality located in the western part of Norway, approximately 200 km south of Ålesund (Figure 7). Jølster became a part of Sunnfjord municipality in January 2020, but for this work, the original Jølster municipality is used. Jølster has an area of 670 km^2 and the altitude range between 208 masl (Jøstervatnet) and 1827 masl (Snønipa). The landscape is mountainous with both steep slope gradients and other places where there are less steep mountain sides covered with vegetation (Hefre et al., 2019). The most common surface material is moraine material (Figure 8). The landslides that most frequently occur in Jølster, especially around Jølstervatnet, are debris- and slush flows (Hefre et al., 2019). In figure 8, potential landslide activity is shown as part of the soil map. The map indicates that Jølster is prone to landslides to a large extent, and in the future, climate changes in this area are expected to increase the frequency of events with heavy rainfall, which can lead to more floods and landslides (Norsk Klimaservicesenter, 2016).

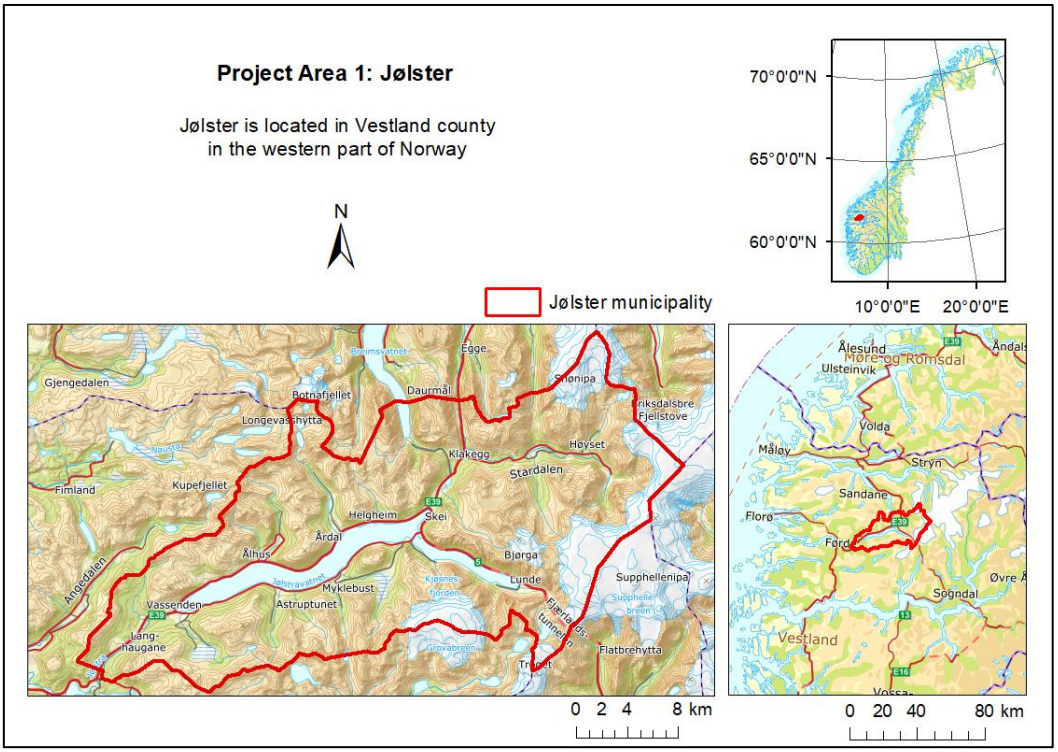

Figure 7: Overview of the main project area, Jølster municipality in Norway. Jølster municipality is marked as a red polygon in the figure where maps are showing the location of Jølster in both Norway and Vestland county.

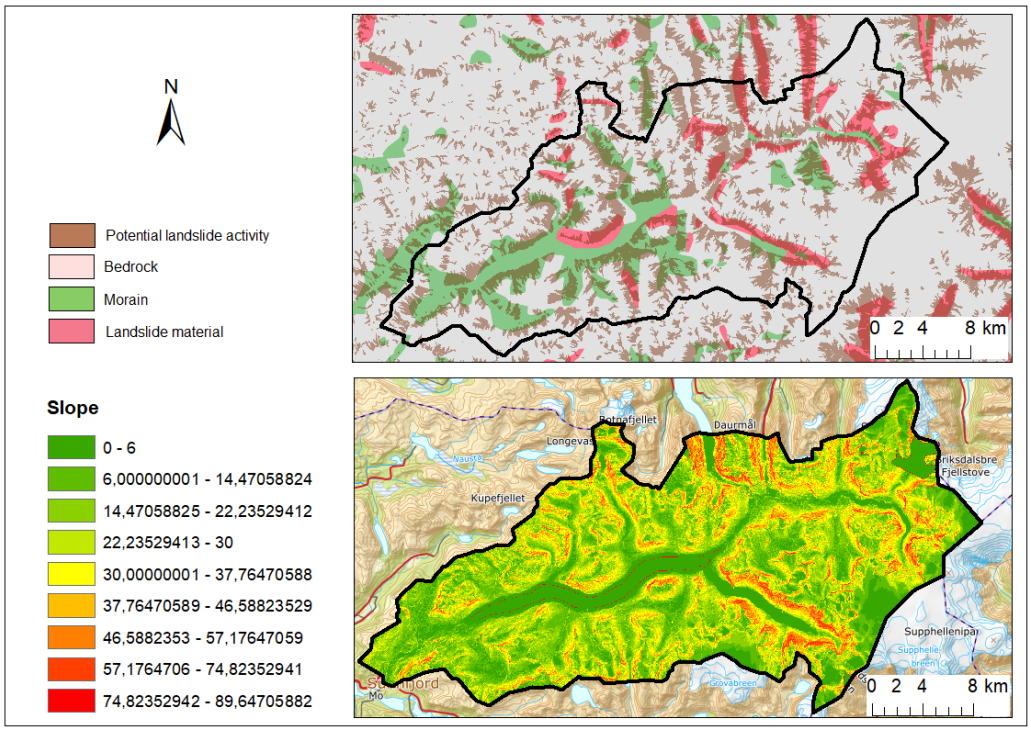

Figure 8: Soil- and slope map over Jølster municipality. The soil map reveals the most common surface material in Jølster municipality, and the soil map shows that several of the valleys in Jølster municipality has a gradient from 30 degrees and above, which is typical slope degrees of where landslides get triggered. The slope map is made from a 10 m resolution DTM and the soil-map is a WMS layer extracted from Geonorge.no. Potential landslide activity is displayed on top of the soil map.

A catastrophic landslide event occurred 30th of July, 2019. Several landslides were triggered after a period of heavy rainfall in Vestland County in Norway. The main types of triggering slope failures were shallow debris slides which caused the destruction of buildings, roads and took one human life. The previous day, MET in corporation with NVE sent out a warning that especially Vestland should expect heavy rain and thunderstorm in addition to strong wind. The intensity and precipitation were bigger than first expected (Agersten et al., 2019). The rain showers were local and at Vassenden in Jølster, 33 mm/hour were registered. There has likely been even more precipitation in the mountains in this area, but no measuring stations are installed here. The strongest wind registered in this area was 20-25 m/s, and was registered at the measure station "Jølster-Kvamsfjellet" which is located at 980 masl (Agersten et al., 2019). Table 3 gives an overview of the reported landslides and affected areas and reveals that Jølster municipality was one of the most affected areas by this event.

Table 3: Overview of the places affected by natural hazards 30. July 2019, in Vestland County. Table modified from NVE (2019).

Affected areas	Municipality	County	Hazard	Consequences
Slåtten	Jølster	Vestland	Debrisflow	Evacuation, damaged buildings
Svidalsneset	Jølster	Vestland	Landslide	Damaged buildings, traffic obstructed
Årnes	Jølster	Vestland	Debris avalanche	Car taken by the landslide
Årdal	Jølster	Vestland	Debris avalanche	Landslide materials on road, traffic obstructed
Årsetelva	Jølster	Vestland	Debris flow	Damaged buildings
Gjesdalelva	Jølster	Vestland	Debris flow	Damaged buildings
Movika	Førde	Vestland	Landslide	Traffic obstructed
Stokkevika	Modalen	Vestland	Landslide	Traffic obstructed
Slottsportentunnelen	Modalen	Vestland	Landslide	Traffic obstructed, evacuation
Hyefjorden	Gloppen	Vestland	Landslide	Landslide materials over Fv 569
Hyen	Nordfjord	Vestland	Flood	Damaged roads, flooded bridge
Holsen	Sunnfjord	Vestland	Flood	Bridge filled with landslide material, raod closed (Fv13)
Åsane	Bergen	Vestland	Local flood	Stores at Gullgruven shopping centre was affected

All Klima 2050 partners including Norwegian Geotechnical Institute (NGI), Norwegian Water Resources and Energy Directorate (NVE), Norwegian Meteorological Institute (MET), and Norwegian University of Science and Technology (NTNU), in addition to the Geological Survey of Norway (NGU) and Western Norway University of Applied Science (HVL) have contributed with research linked to the Jølster event. Data retrieved is collected by GPS measurements, helicopter, geological field survey, drones, and satellites (Strout & Devoli, 2020).

Both NGI and HVL have worked together on estimating landslide volumes. They have used drones and have available data for most of the landslides in the area. DTMs can be extracted from this data and can further be used to estimate volumes of the landslides. Field surveys and observations were done in Jølster where especially erosion in earlier landslide areas has been studied. With today's models, it is not possible to define a classic triggering point, in addition, it is in general difficult to model events that started as a flow, water bringing rocks, and further land masses (Strout & Devoli, 2020).

Moreover, several bachelor studies, master studies, and Ph.D. study has analyzed the Jølster event. Especially Ph.D. Candidate Erin Lindsay's work is important for this thesis. Lindsay's work is described under section 1.3 Background, as part of the Introduction.

This master thesis will focus on landslides triggered by heavy rainfall and the Jølster event will be used to investigate the use of optical RS data and vegetation indices. To make sure the quality of the method does not get affected by the location or size of the landslide, a second study area is introduced.

4.2 Oso, Washington

The second location introduced in this master thesis is Oso located in Washington, USA (Figure 9). Oso is a part of Snohomish County and has an area of 9.6 km^2. The climate is humid, similar to the climate in Jølster. Northeast of Oso, a terrace slope that has experienced several landslides is located (Aaron et al., 2017). The terrace slope has different plateaus, with the Whitman bench at the top approximately 270 masl, and the Ancient Landslide Bench, at an altitude of 180 masl. The terrace stratigraphy from the bottom up consists of sands and gravels, glaciolacustrine silt and clay, advanced outwash sand, and till at the top which is periodically covered by recessional outwash of sand (Figure 10) (Stark et al., 2017).

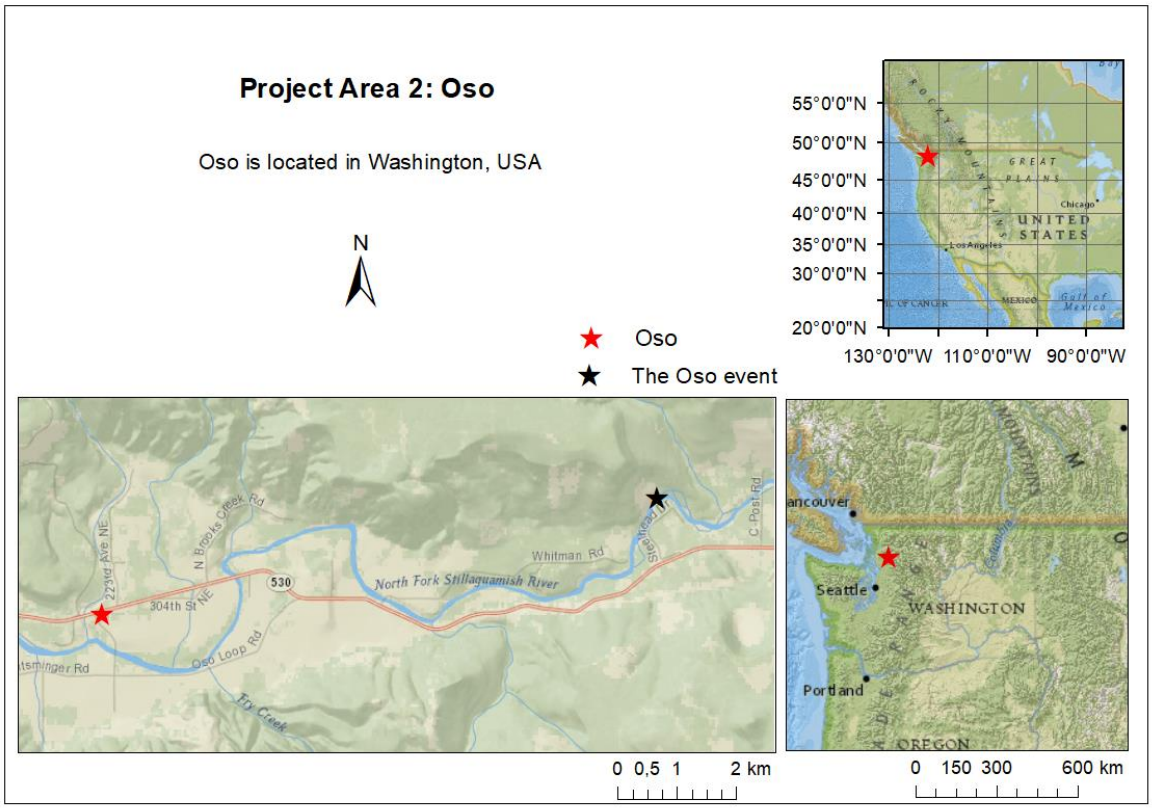

Figure 9: Overview of the second project area, Oso located in Washington, USA. The red star indicates the location of Oso, and the black star indicates the location of the Oso landslide event in 2014, northeast of Oso.

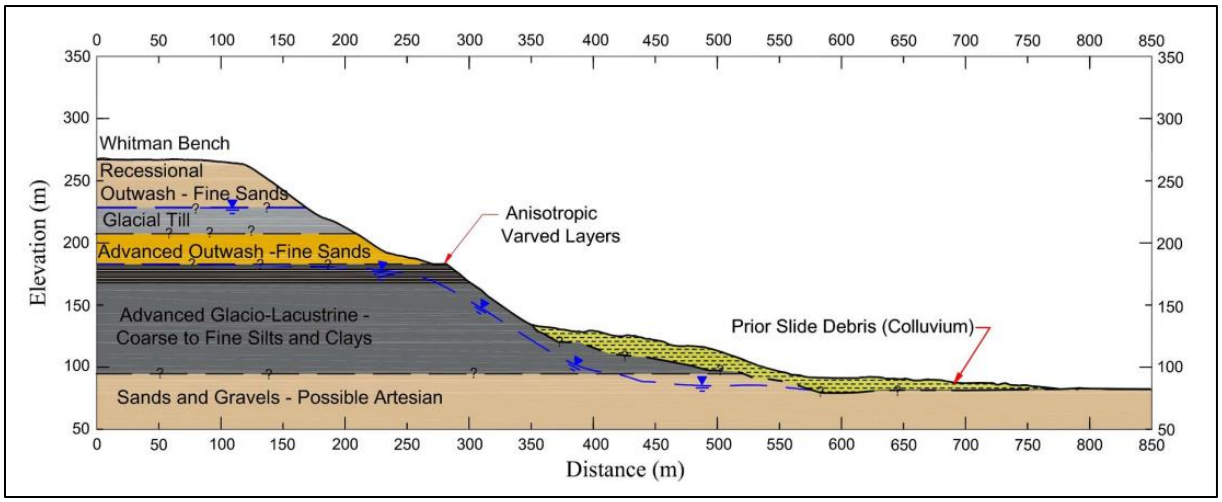

Figure 10: Slope cross-section showing the stratigraphy of the terrace northeast of Oso. The blue line indicates the ground water table. Figure retrieved from Stark et al. (2017).

On 22nd of March, 2014, a catastrophic landslide event occurred northeast of Oso. A terrace slope failed and caused 43 fatalities, road destruction, and damaging civilian property (Aaron et al., 2017). Steelhead Haven Community was destroyed (suffered from extreme damage), and the landslide buried the Washington State Route 530 (Stark et al., 2017). The landslide also crossed the North Fork Stillaguamish River and dammed it (Wartman et al., 2016). This area has a history of landslide events, but the 2014 event had a different failure behavior and traveled nearly 1.4 km, on a runout surface close to horizontal, acting like a flow slide (Aaron et al., 2017). According to Wartman et al. (2016), the landslide would be classified as a debris flow slide by using the updated landslide classification, originally by Varnes (Figure 3). Unlike most other known failures in this terrace slope, this landslide initiated at the top plateau, the Whitman Bench (Aaron et al., 2017), and had this large spatial extent in runout due to the higher elevation (Stark et al., 2017). The total volume of the landslide was estimated to be near 8.3 million m^3 (Stark et al., 2017; Wartman et al., 2016). In the days before the event, the precipitation was unusually intense, and according to precipitation gauges in the area, this period of rainfall was significantly higher than the average. The rainfall in March leading up to the landslide event is proven to be the wettest time period in 86 years, according to historical meteorological data (Stark et al., 2017). The event in 2014, is known to be the most deadly event the continental Unites States has experienced (Wartman et al., 2016). This event will hereby be referred to as the Oso event.

With the same triggering mechanism and climate, this event is well suited to be used as a validation site for the method applied to the Jølster event.

Several studies have analyzed the Oso event in 2014, and it is well documented through obtaining high-resolution topographic LiDAR data, aerial photo imagery, and field surveys. Earlier events on the case site are also investigated, and the data source most commonly used to reconstruct the landslides deposits morphology is LiDAR pre- and post-topographic data (Aaron et al., 2017). LiDAR can be used to generate topographic relief images with high resolution, useful for revealing historical landslides (Haugerud, 2014; Stark et al., 2017). According to the LiDAR data, there have been several repeating landslides in the area of the Oso event in 2014 (Haugerud, 2014; Stark et al., 2017; Wartman et al., 2016). These historic events are varying in size, both large, similar to the 2014 event which initiated in the upper part of the terrace, and smaller landslides in the lower part of the slope usually caused by river erosion and precipitation (Stark et al., 2017). LiDAR surveys were conducted for the area in 2003 and 2013, in addition to 2014 after the 2014 event (Aaron et al., 2017), and by looking at the difference in slope topography between these images, accumulation zones and extent could be revealed (Stark et al., 2017). Through information retrieved from LiDAR data, it was found that pervious landslides between 1937 and 2006 initiated at a lower part of the terrace slope. Changes in the Stillaguamish river were also detectable, which revealed important information about return periods of landslides at this case site by looking at areas where the river had caused a reduction in the landslide bench, and erosion on the landslide masses (Stark et al., 2017).

Aerial photographs have also been used to study the Whitman Bench plateau (Stark et al., 2017; Wartman et al., 2016), and showed that the terrace slope had been stable for approximately 100 years (Stark et al., 2017). Results from aerial photographs show that most of the previous landslides only involved glaciolacustrine deposits, indicating that they initiated in the lower part of the terrace. Some of the Ancient Landslide bench was removed by these landslides, but the bench still supported the Whitman bench until the landslide in 2006. These previous landslides also moved the still river, and after the landslide in 2006, the river channel was moved far south of the slope, which indicates that river erosion did not initiate the Oso event in 2014 (Stark et al., 2017).

Several field investigations have also been carried out, where especially information from boreholes has been of great importance for finding information about the terraces stratigraphy (Aaron et al., 2017). Moreover, a meteorological overview of the conditions before the event in addition to information about historic events on the site, and geomorphology conditions were given by Wartman et al. (2016). They interpreted the failure mechanism by analyzing seismic

signals from the slide in combination with field observations, concluding that the landslide had two movement phases.

The study of Sun et al. (2015), has proven that also interferometric synthetic aperture radar (InSAR) is useful for landslide detection, for landslides such as the Oso event in 2014, analyzing movements in the terrace slope before the event. Deformation maps derived from InSAR data indicated that the slope where the Oso slide in 2014 occurred was active between 2007 and 2011 (Sun et al., 2015).

In summary, several approaches are used to collect information about landslide events in the terrace north-east of Oso. To my best knowledge, throughout a broad spectrum of literature, no earlier studies have focused on optical satellite sensors and vegetation indices for mapping the Oso landslide in 2014.

5 Method

5.1 Data collection

In this study, pre- and post-event 12 bit Sentinel 2A images acquired 2019.07.28 and 2019.08.27, in addition to a second post-event Sentinel 2B image acquired 2019.08.02 (YYYY.MM.DD) were used for the landslide mapping in Jølster municipality in Norway, and comparison between different vegetation indices. The 10-meter multispectral bands were utilized for this study. Both Sentinel 2 level 1 (L1) and Sentinel 2 level 2 (L2) were acquired to compare the two levels released to users.

Landsat 8 pre- and post-images were also acquired for both Jølster and Oso, to compare the use of two different optical satellites on the Jølster event, in addition, to analyze the Oso event with optical satellite data. Sentinel 2 data was not yet available at the time of the Oso event. Landsat 8 images from the dates 2019.07.11 and 2019.08.03 were acquired for the Jølster event and 2014.01.18 and 2014.04.01 (YYYY.MM.DD) for the Oso mudslide in Washington. Only L1 data from Landsat 8 is acquired, and the 30-meter multispectral bands were utilized.

Satellite images from the Sentinel 2 constellation were downloaded from the Copernicus Open Access Hub. Copernicus Open Access Hub is developed by the European Space Agency (ESA) and provides a complete database of satellite images from Sentinel 1, Sentinel 2, and Sentinel 3. The website provides an easy-to-use, open, and free access platform for collecting satellite images. In the Advanced Search, there are two alternative settings where the dates of interest can be chosen, namely the sensing period and the ingestion period. The sensing period represents the time when the image was taken from the sensor while the ingestion period represents the time when the image was available online. The sensing period was set one month before the event and one month after the event. The satellite platform chosen was S2A_* and S2B_*, and the product type was set to be S2MSI1C for L1 data, and S2MSI2A for L2 data. Further, a polygon was drawn around the area of interest which is Jølster municipality. This was done to limit the results and the program searched for images that only cover the polygon. The chosen images were based on those with the smallest percent of cloud cover among the alternative images in the search. Sentinel 2A pre-image was not affected by clouds, but both the post-images were to some degree affected by clouds.

Landsat 8 images were downloaded from USGS Earth Explorer. A polygon was drawn around Jølster in addition to Oso, in two different steps, to limit the extent. In the dataset folder, Landsat 8 OLI/TIRS C1 Level-1 was chosen. No additional criteria were set. The chosen images were

based on those having the smallest percentage of cloud cover. The satellite images produced by Landsat 8 retrieved for this study had no cloud cover in the area of interest.

5.2 Software

The software package ArcMap was used in this thesis to visualize data, spatial analysis and create maps and datasets. ArcMap is a part of the traditional ArcGIS Desktop, developed by the Environmental Systems Research Institute (ESRI), for the purpose of creating maps, spatial analysis, and geographic data management (ESRI, 2020). Further descriptions of how ArcMap is used in this study for calculating vegetation indices and mapping landslides can be found in Section 5.3. All the maps without further references are created by this paper's author in ArcMap.

ArcGIS Pro is a new version of ArcGIS desktop and was used to remove clouds from the satellite images.

In addition, Microsoft Excel is used for simple statistical analysis and sorting of data. All the tables in the thesis are created in Excel.

5.3 Analytical approach

After downloading the Sentinel 2 and Landsat 8 satellite images, they were imported to ArcMap for visualization. Since the area of interest is a historical municipality, a WMS layer from Geonorge showing historical municipalities was added to the GIS project to draw a polygon around Jølster. Once the polygon of Jølster was produced, the satellite images were clipped to the area of interest.

A subset of vegetation indices found in literature was calculated by using the tool Raster Calculator. The vegetation indices calculated for observing changes in vegetation were Normalized Difference Vegetation Index (NDVI), Green Normalized Vegetation Index (GNDVI), Enhanced Vegetation Index (EVI), and Atmospherically Resistant Vegetation Index (ARVI).

The vegetation indices calculated in this study were chosen based on the limitations of NDVI. In Kaufman (1988) and Slater (1980), it is explained that the Red and NIR bands used in NDVI suffer from atmospheric effects. Both ARVI and EVI correct the NDVI for atmospheric influence and were therefore calculated. Further, since the detection of landslides with smaller areas is a limitation both for Sentinel 2 and Landsat 8, GNDVI was calculated and Hölbling et

al. (2015) argue that this vegetation index improved the detection of small-scale changes that NDVI does not capture.

The vegetation indices and their equations are as follows:

Normalized Difference Vegetation Index:

$$NDVI = \frac{(\mathrm{NIR} - \mathrm{Red})}{(\mathrm{NIR} + \mathrm{Red})}$$

Green Normalized Vegetation Index:

$$GNDVI = \frac{(\mathrm{NIR} - \mathrm{Green})}{(\mathrm{NIR} + \mathrm{Green})}$$

Enhanced Vegetation Index:

$$EVI = 2.5 * \frac{(\mathrm{NIR} - \mathrm{Red})}{(\mathrm{NIR} + (\mathrm{C1} * \mathrm{Red}) - (\mathrm{C2} * \mathrm{Blue}) + \mathrm{L})}$$

Where C1 and C2 coefficients for correcting aerosol scattering, and L adjusts for canopy background (EOS, 2019). The same value for these three factors as used for MODIS-EO can also be used for Sentinel 2 and Landsat 8, which are C1 = 6, C2 = 7.5, and L = 1.

Atmospherically Resistant Vegetation Index:

$$ARVI = \frac{(\mathrm{NIR} - \mathrm{Red} - \mathrm{y} * (\mathrm{Red} - \mathrm{Blue}))}{(\mathrm{NIR} + \mathrm{Red} - \mathrm{y} * (\mathrm{Red} - \mathrm{Blue}))}$$

In this study y = 1 is used, as shown in Kaufman and Tanre (1992) to be the optimum value for RS applications, especially when information about aerosol type is missing.

In addition to vegetation indices, two water indices were calculated: the Normalized Difference Water Index (NDWI) and the Land Surface Water Index (LSWI). These were calculated because debris flows often follow rivers and contain a large amount of water (NVE, 2020b).

The water indices and their equations are as follows:

Normalized Difference Water Index:

$$NDWI = \frac{(\text{Green} - \text{NIR})}{(\text{Green} + \text{NIR})}$$

Land Surface Water Index:

$$LSWI = \frac{(\text{NIR} - \text{SWIR})}{(\text{NIR} + \text{SWIR})}$$

For Sentinel 2, Near Infra-Red (NIR) corresponds to band 8, Red to band 4, Green to band 3, Blue to band 2, and SWIR to band 11. Band 12 is also in the SWIR range, but band 11 is chosen because it has a closer spectral location to the other bands in the formula (Table 1). For Landsat 8 the red, green, and blue correspond to the same bands as for Sentinel 2, while NIR corresponds to band 5 and SWIR corresponds to band 6 (Table 2).

The indices were calculated for both the pre- and post-image. By subtracting pre from post with the tool MINUS the difference was calculated and the total change was discovered. The result from ARVI and NDVI calculation for a given pixel always ranges between +1 and -1, where numbers close to +1 represent a high presence of green leaves, and a value of zero indicates no vegetation. In other words, after subtracting pre- from post-images, negative values represent areas that have undergone changes and a more positive value represents an area with the same condition in the pre-and post-image. The difference in vegetation indices between the pre- and post-image will herby be referred to as (for example) dNDVI.

All the six indices introduced were applied to the Jølster case site for initial evaluation. dNDVI and dARVI gave landslide values with the greatest contrast to the surroundings compared to the other vegetation indices calculated. Therefore, it was decided to continue with dNDVI and dARVI for further analysis for landslide change detection and mapping. dNDVI and dARVI

were then calculated for the Oso case site, to conduct a comparative evaluation in an additional area.

An overview of the workflow in Model Builder for calculating the difference in the vegetation indices is shown in figure 11.

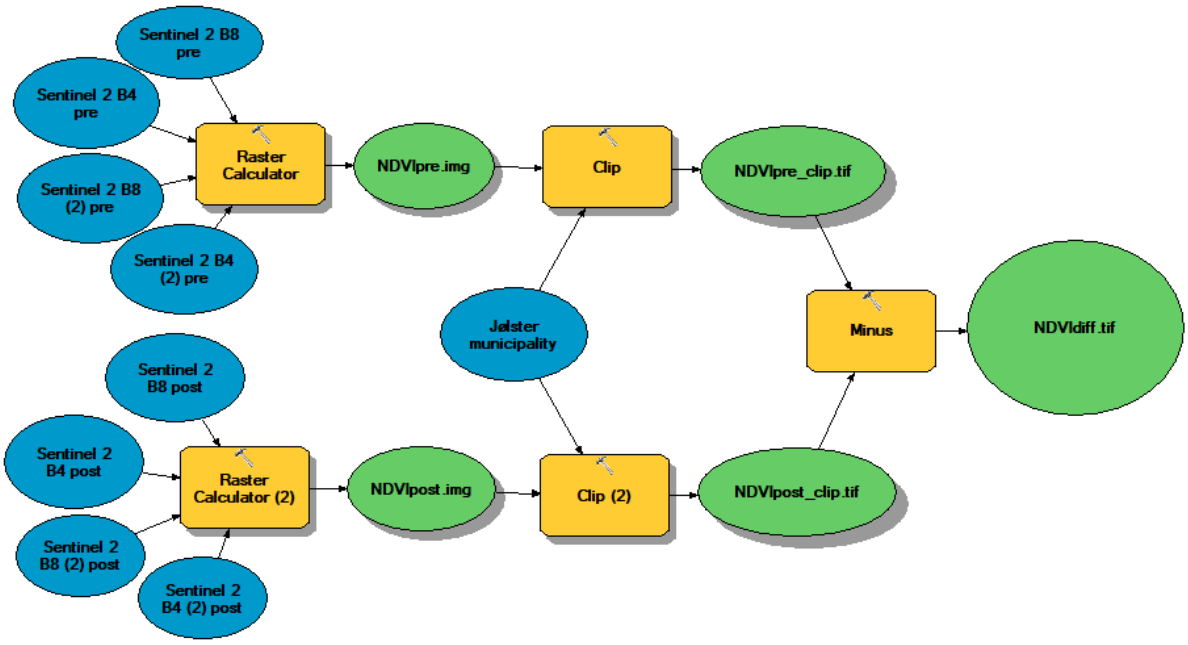

Figure 11: Overview of the workflow for calculating NDVI and dNDVI. The same workflow is used for all vegetation indices and both levels of data, in addition to Landsat 8 data. With Landsat 8 data, band 8 is switched with band 5 for calculating NDVI, which is the red band for Landsat 8.

With the use of dNDVI and dARVI, both a manual and a semi-automatic approach to identify landslides were undertaken in Jølster municipality. These approaches will be described in the two following subsections. For the Oso event, only the comparative evaluation of dNDVI and dARVI's ability to recognize changes caused by the landslide in 2014 was conducted.

5.3.1 Manual Landslide Mapping

A manual recognition of landslides in Jølster municipality was done by systematically looking at areas with a low pixel value in dARVI calculated with Sentinel 2, L2 data. The intention behind the manual mapping was to provide the number of landslides dARVI contributed to identifying. Large negative values indicate change between pre-and post-image, which is expected for areas affected by landslides. The color range to display the indices goes from green (no change in vegetation = positive value) to red (change in vegetation = negative value).

Elongated clusters of red pixels, which could potentially indicate a strip of removed vegetation, were evaluated.

With the use of two post-event images, the manual mapping was done in two rounds. First, with Sentinel 2A post-image, then with Sentinel 2B post-image. The two images were not affected by clouds in the same area. The use of both the post-images in the manual mapping allowed a more precise mapping.

Several areas showed low dARVI pixel value. The areas showing low value, but still not distinguishable as a landslide were evaluated by looking at natural color image composites. If the RGB image presented evidence for debris accumulation, it was marked as a landslide. For instance, rivers were some of the objects showing low values, with the same shape as expected for landslides. Only those parts that exhibited an increase in sediments in the river, and where the sediments took a new path than the original river path, were mapped as landslides. The landslides were mapped by producing a polygon around the outline of these areas which represented a change.

In the attribute table of the mapped landslides, information was added for further statistical analysis. The landslide areas were calculated. In addition, it was noted if the landslides were either following a river, crossing a river, or had their origin in, or at the end of the river. This was done by studying a topographic map used as a background map, combined with a shapefile containing rivers was downloaded from “nedlastning.nve.no”.

Moreover, to add supplementary information about elevation and slope, digital terrain model (DTM) with a 1-meter resolution, were downloaded from hoydedata.no. These DTMs, where each covered parts of Jølster municipality, were first resampled in ArcMap to 10 meters, and afterward merged by using the tool “Mosaic To New Raster”. The best resolution of the satellite images is 10 meters, and for this study, it was concluded not necessary to have a DTM with a higher resolution. A DTM with a higher resolution is also more time-consuming to work with. Further, the tool “Slope” was used on the DTM to make a slope map. Both the slope map and the DTM were clipped to the polygon of Jølster municipality. Further, the “Identify” tool in ArcMap was used to collect information concerning the elevation and slope from which the landslides were initiated, as well as the slope runout. Elevation was extracted from the DTM, and the slope was extracted from the slope map.

For a comparison between dARVI and dNDVI, the mapped landslide polygons were displayed on top of dNDVI also calculated with Sentinel 2 L2 data, to see if there was any difference in

where low values clustered, if dNDVI mapped different landslides, or if the mapped landslides had another spatial distribution. To compare pixel values of both dARVI and dNDVI inside the landslide polygons, the tool “Zonal Statistics as Table” was used to summarize the values, and further, the tables were converted to Excel. The attribute table for the landslide polygons was also transferred to Excel. The tool “Zonal Statistics as Table” was also used to extract the pixel values of dARVI and dNDVI in the landslide triggered by the Oso landslide event in 2014. This was done to evaluate the difference in how dARVI and dNDVI maps change at a second location.

Further, in Excel, different combinations of the data were put together, trying to discover the difference in mapping between dARVI and dNDVI. For comparing dARVI and dNDVI, ([dARVI mean value] – [dNDVI mean value]) was calculated for all identified landslides. By subtracting the mean value of dNDVI from the mean value of dARVI, a comparison of the landslide evaluation by the two indices was enabled. In the case of a positive difference between the two mean values, dNDVI contains the lowest value. In the case of a negative difference between the two mean values, dARVI has the lowest value.

Moreover, the landslide polygons were also displayed over dARVI calculated with Landsat 8 data, and the same comparison as between dARVI and dNDVI calculated with Sentinel 2 data was undertaken; does dARVI calculated with Landsat 8 data map the same landslides as dARVI calculated with Sentinel 2, and is the spatial extent the same?

The manually mapped landslides were lastly compared to the landslides registered in NVEs landslide database from after the Jølster event in 2019. By downloading the landslide database from “nedlastning.nve.no”, the landslides from this specific event were selected by looking at the date, and further, they were displayed on top of the landslides mapped in this study.

5.3.2 Landslide mapping in Raster Calculator

An attempt to semi-automate the approach for mapping landslides was done in Raster Calculator. The RS images, produced by Sentinel 2, collected for this study were affected by clouds, so in advance of a more automated attempt for mapping landslides, these had to be removed.

Several approaches to remove the clouds were tried, and in this study, two different methods are used. First, Pixel Editor in ArcGIS Pro was used to remove clouds in Sentinel 2A post-image. With this approach, the cloud-affected area can be replaced with a cloud-free image taken at another time. In this case, both Sentinel 2B and Landsat 8 post-image can be used due

to no cloud cover in the same area that Sentinel 2A post-image is affected. However, the spatial resolution and bandwidths must be the same to seamlessly merge the cloud-free image into the base map, and Sentinel 2B is therefore utilized. With the use of Pixel Editor, a polygon was drawn around the area affected by clouds and further chose the cloud-free image as the source layer and replace it. Further, the color of the base map and reference map was matched.

The second approach for the removal of clouds was done in Raster Calculator, where logical operators were used to excluding pixel values representing clouds. This approach was applied to the difference image between Sentinel 2A pre-image and Sentinel 2B post-image. The pixel values representing clouds were identified by utilizing the identification tool. Band 2 (blue), which gave the largest contrast between the cloud and the surroundings, was used. The clouds present in the Sentinel 2B post-image had a distinct outline and the pixels representing clouds were much brighter than the other elements in the scene. Only pixels representing clouds had a pixel value greater than 3000 and this was added to the final equation in Raster Calculator for landslide mapping in Jølster municipality.

With cloud-free Sentinel 2A post-image, dARVI was again calculated with the same approach as in figure 11, but this time, with the new cloud-free image used as post-image. Keeping in mind that a distinct change in dARVI- or dNDVI-value does not necessarily represent landslides, but the overall change between pre-and post-image, several assumptions had to be made to extract only landslide information. Logic operators in Raster Calculator were therefore used to define what is a landslide and what are other changes caught by the remote sensor. The values inside the landslide polygons had a wide range, revealed by the “Identify” tool. It was therefore decided to use values extracted from the table showing dARVI values inside the landslide polygons, previously developed by “Zonal Statistics as Table”. This was done assuming that the dARVI values inside the landslide polygons were sufficiently representative of the typical conditions.

In Raster Calculator two equations were run to detect landslides. The first equation included dARVI value as the difference between ARVI calculated with Sentinel 2A pre-and post-image, and the second equation included dARVI value as the difference between ARVI calculated with sentinel 2A pre-image and Sentinel 2B post-image. The dARVI values inside the landslide polygon ranged from +0.9 to -1. From the values in Excel, it was decided to use -0.2 as the highest dARVI value that would be detected. The average mean value to the landslides with the use of both Sentinel 2A- and Sentinel 2B post-images was below -0.2, in addition, most of the

landslides had a min value below -0.2. With the use of dARVI < -0-2 in the Raster Calculator, most of the landslides would be represented.

Further, from the landslide attribute table, it was found that the max slope where the landslides initiated was 54.25 degrees. Slope < 54.25 was therefore added to the equation, excluding all areas steeper than this. Moreover, from the landslides attribute table, all landslides appear under 1336 m, and DTM < 1336 was supplemented to the equation. Because shadow was still present in the result, band 2 was used to remove these areas by applying Band 2 > 500. Furthermore, rivers were some of the objects having similar values to landslides, and the water index NDWI was therefore used to exclude rivers, but not landslides, by applying dNDWI > 0.3 to the equation.

Moreover, there was still an overrepresentation of false positives, i.e., information in the result which did not represent landslides. With the use of Sentinel 2A post-image, especially crop fields and landslides had the same range of values. To separate them, Slope > 15 degrees was used as most of the crop fields had a slope beneath this. This was only added to the equation where the Sentinel 2A post-image was used. For the calculation where the Sentinel 2B was used as post-image, Band 2 < 3000 was added to the equation due to the removal of clouds.

The final equations used in Raster Calculator are as follows:

- Equation 1: (S2A_dARVI < - 0.2) & (Slope < 54.25) & (Slope > 15) & (DTM10m < 1336) & (Band 2 > 500) & (dNDWI > 0.3).
- Equation 2: (S2B_dARVI < - 0.2) & (Slope < 54.25) & (DTM10m < 1336) & (Band 2 > 500) & (Band 2 < 3000) & (dNDWI > 0.3).

6 Results

In this section, the results will be presented. This includes results of the difference in the vegetation indices NDVI and ARVI at both case sites, with the use of both different processing levels of data and different satellite sensors. Further, the results from the manual mapping and the mapping done in Raster Calculator will be presented.

6.1 Vegetation indices - Jølster

6.1.1 ARVI and NDVI differences calculated with Sentinel 2

In the initial inspection of the dARVI display in figure 12, some differences are detected between the use of L1 data and L2 data. L1 data highlight more objects, like water and shadows. Water with L2 data is also marked as a great contrast to the surroundings, but most of the water has pixel values closer to zero compared to L1 data. There are two clouds present in the scene, one in the southeast end of the lake Jølstervatnet, and another further northeast. Both clouds are visible in both displays as a cluster of pixels with negative values. The cloud northeast of the lake is harder to detect in the display of L1 data where it is surrounded by shadows also with similar negative pixel values. Moreover, only L1 maps the cloud shadows. Both levels map crop fields with negative values, where L1 is noisier than L2.

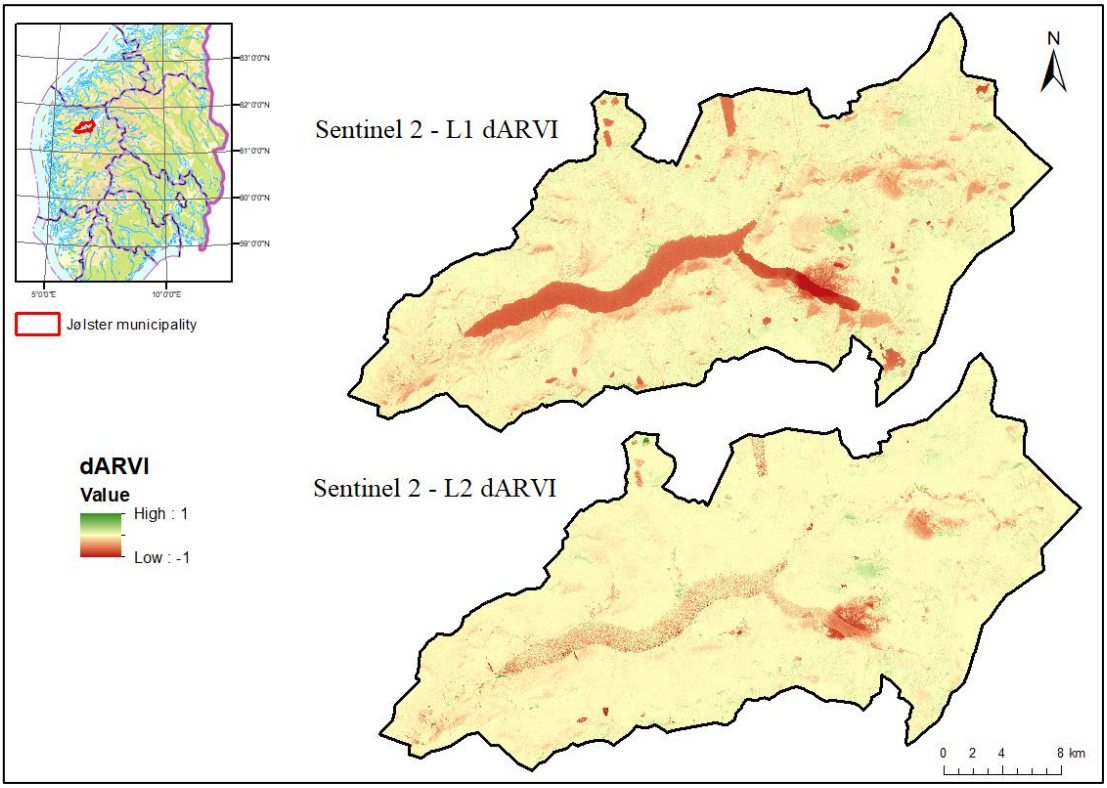

Figure 12: Calculation of dARVI with Sentinel 2A L1- and Sentinel 2A L2 data. The vegetation index is displayed for Jølster municipality, and its location is shown in the overview map in the upper left corner. The dynamic range for dARVI is 1 to -1.

The results of the dNDVI calculation with both L1 and L2 data are displayed in figure 13. The result is similar to the results from dARVI (figure 12). Both levels map the clouds, but only L1 maps the cloud shadows. In addition, L1 maps more shadows in the mountainsides around the lake, similar to the results from dARVI. Crop fields stand out with negative pixel values. In contrast to the calculation of dARVI, L1 does not highlight water with negative values, but L2 does. Both levels also get a higher value for water compared to dARVI, in L1 approximately a value of zero and even positive value in L2. In addition, the calculation of dNDVI maps more of the ice and snow along the east side of the polygon compared to dARVI.

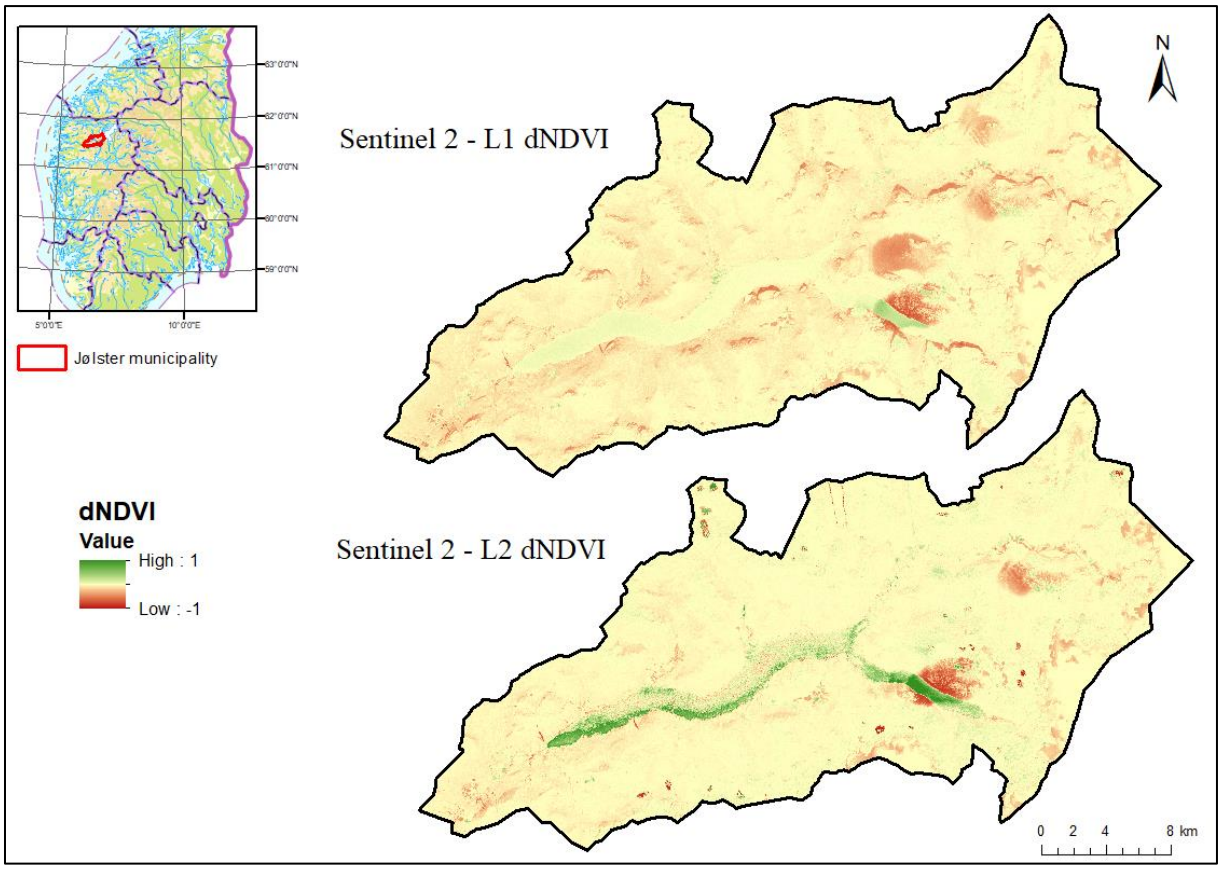

Figure 13: Calculation of dNDVI with Sentinel 2A L1 - and Sentinel 2A L2 data. The vegetation index is displayed only for Jølster municipality, and its location is shown in the overview map in the upper left corner. The dynamic range for dNDVI is 1 to -1.

6.1.2 ARVI and NDVI differences calculated with Landsat 8

The calculation of dARVI with the use of Landsat 8 data is displayed in figure 14, and figure 15 displays the calculation of dNDVI calculated with Landsat 8 data. In contrast to the calculations done with Sentinel 2A data, more areas in Jølster municipality show greater positive pixel values presented in green color. These areas mainly represent crop fields that had a strong negative value in Sentinel 2 index differences. In general, both dARVI and dNDVI with the use of Landsat 8 data show fewer areas with strong negative values. Shadow is present

along hillsides, but the results are remarkably less affected by shadow compared to index differences with Sentinel 2A L1 data. Moreover, there is less difference between dARVI and dNDVI calculated with Landsat 8, L1 data than between dARVI and dNDVI calculated with Sentinel 2A, L1 data.

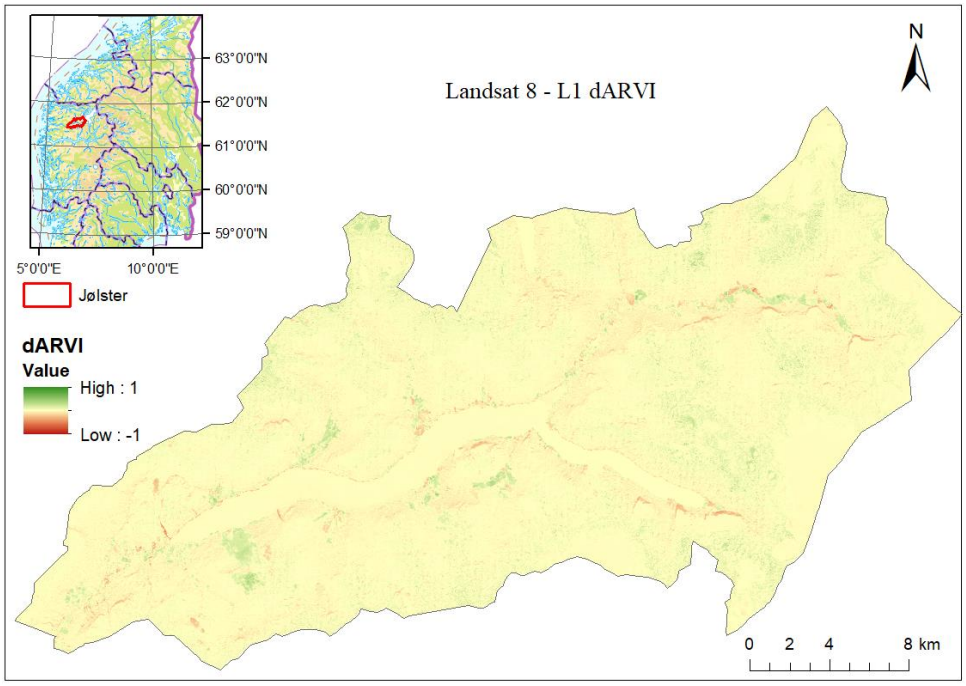

Figure 14: Displays dARVI calculated with Landsat 8 data. The vegetation index is displayed only for Jølster municipality, and its location is shown in the overview map in the upper left corner. The dynamic range for dARVI is 1 to -1.

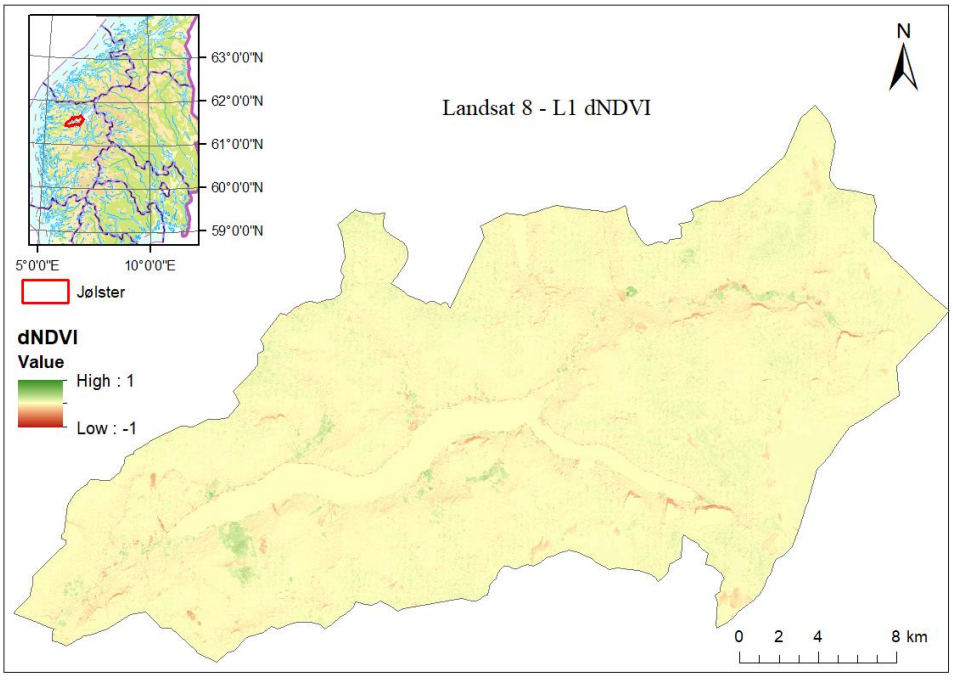

Figure 15: Displays dNDVI calculated with Landsat 8 data. The vegetation index is displayed only for Jølster municipality, and its location is shown in the overview map in the upper left corner. The dynamic range for dNDVI is 1 to -1.

6.2 Landslides and other elements of interest

Both dARVI (L1 and L2) and dNDVI (L1 and L2) calculated with Sentinel 2 and Landsat 8, highlights landslides. However, there are differences in the required size of the landslide for the vegetation indices to give a distinct signal of change. Figure 16 contains four maps where dARVI and dNDVI calculated with Sentinel 2A, L1 and L2 data, are displayed. The four maps in figure 16, represent a comparison of an enlarged section of the mountainside above Vassenden in Jølster municipality, where several landslides got triggered as part of the event 30. July 2019. In all four maps, the largest landslide is easily detected, where map B (dARVI, L2 data) gives the lowest value inside the landslide, creating the largest contrast between the landslide and the surroundings. Besides this landslide, there are several smaller landslides further south along the mountainside. Map B (dARVI, L2 data), C (dNDVI L1 data), and D (dNDVI L2 data) show clear traces of these smaller landslides, while in map A (dARVI L1 data), they are more difficult to recognize. In summary, all the different combinations of dARVI and dNDVI with different levels of data, show a distinct disruption in vegetation, but for smaller areas (only a few pixels), dARVI (L2) showed the strongest change to the surroundings.

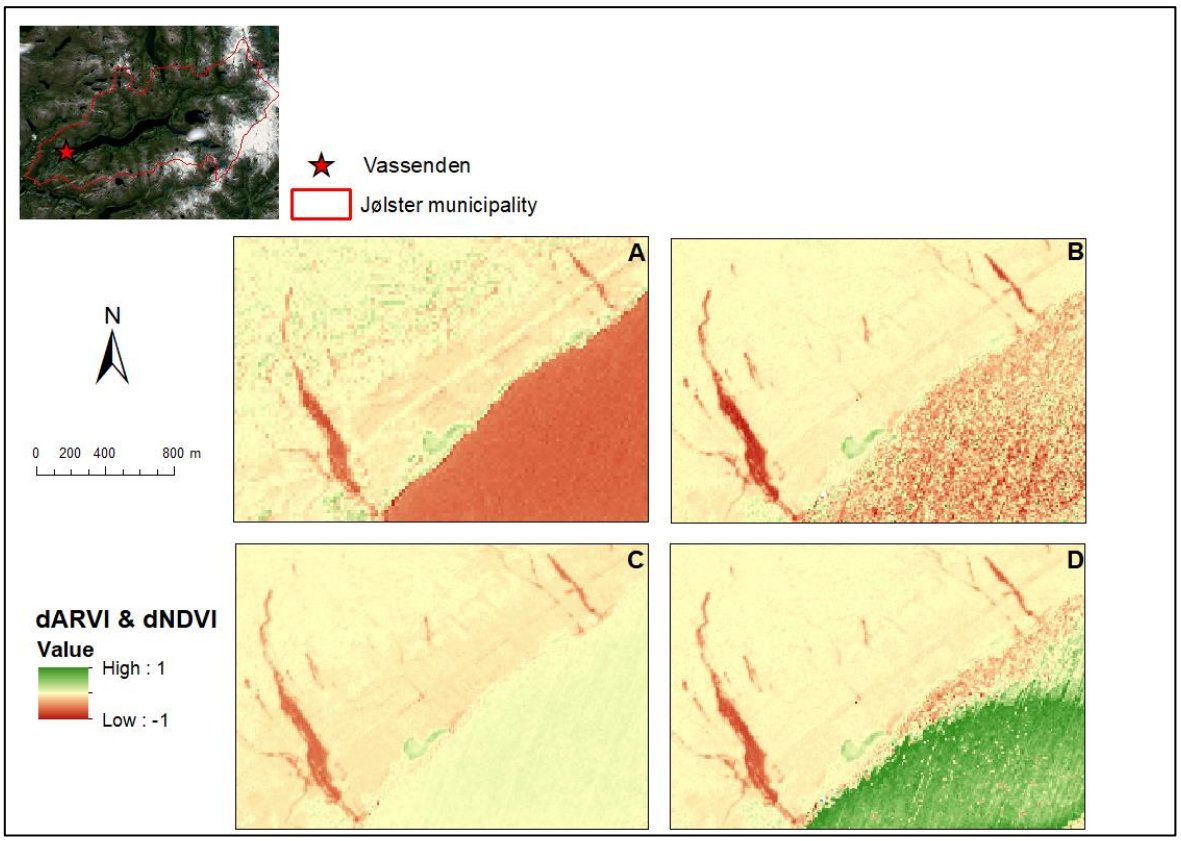

Figure 16: An enlarged section of Jølster municipality is shown in A, B, C, and D, displayed with dARVI and dNDVI calculated with Sentinel 2 data. The section is from a mountainside above Vassenden, in Jølster municipality, marked as a red star in the overview map in the upper left corner. Map A and B display the vegetation index dARVI, and map C and D displays dNDVI. L1 data is used in map A and C, while L2 data is used in map B and D.

Moreover, calculation of dARVI and dNDVI with the use of Landsat 8 data also maps landslides, but slightly poorer than the calculation with Sentinel 2 data. Figure 17 shows the same enlarged section of Jølster municipality as in figure 16. The largest landslide in Vassenden is still easily recognizable, but the smaller landslides, further east, are not. There are several places with scattered low pixel values, but not distinct elongated clusters.

Figure 17: Displays dARVI and dNDVI calculated with Landsat 8 data for an enlarged section of Jølster municipality. The section is from a mountainside above Vassenden, marked as a red star in the overview map in the upper left corner.

Except for the poorer resolution, two of the main differences using Landsat 8 data instead of Sentinel 2A is that Landsat 8 images retrieved for this study have a shorter revisiting time between pre-and post-image, and do not contain clouds in the same area as Sentinel 2A.

In figure 18 an enlarged visual presentation of the location containing clouds in Sentinel 2A is displayed with both dARVI and dNDVI calculated with Landsat 8 data, in two different maps. There is a limited difference between the two displays and several places with low pixel values but it is noisy. By comparing those areas with low values for the index differences with an RGB image, any potential landslide in this location would be detected. No landslides were mapped here.

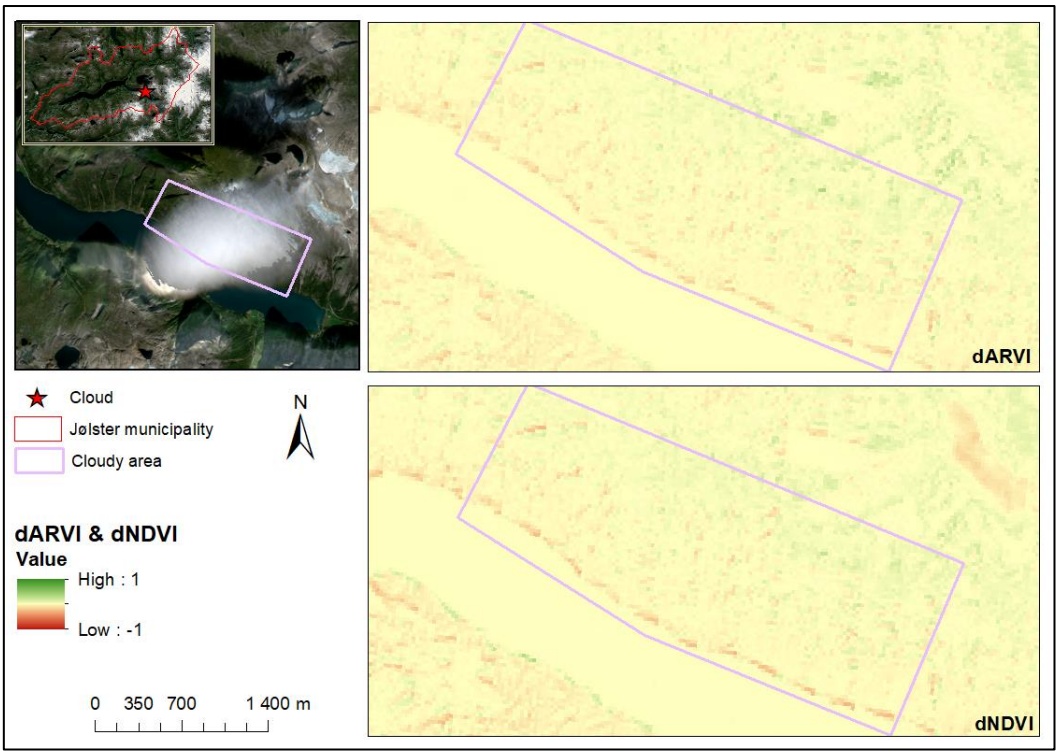

Figure 18: dARVI and dNDVI calculated with Landsat 8 data displayed over the cloud-affected area in Sentinel 2A.

In figure 19, an enlarged section of the western part of Jølster municipality is displayed using dARVI calculated with both Sentinel 2A L1 and L2 data, and Landsat 8 L1 data. Two differences between mapping with Sentinel 2 data and Landsat 8 data is the mapping of water and crop fields in opposite ways. When using Sentinel 2 data, both L1 and L2, water is presented with positive value while mapping with Landsat 8 data water is presented with negative values. However, this is the opposite for the lake Jølstervatnet, present in figure 12 and 14, where Sentinel 2 data mapped the lake with negative values while Landsat 8 data mapped the lake with more positive values. Moreover, Sentinel 2 maps crop fields with negative values, while Landsat 8 maps them with positive values. Further, the results indicate that Landsat 8 is less affected by shadows when Sentinel 2 also shows the presence of haze in the same area. There are major differences in how landslides are mapped. Level 2 data map significantly more accurate than level 1 data, by giving the landslides more coherence in negative values. Especially by providing increasingly strong contrast from landslides and their surroundings. Moreover, dARVI calculated with Sentinel 2 L1 highlights landslides better than dARVI calculated with Landsat 8 L1.

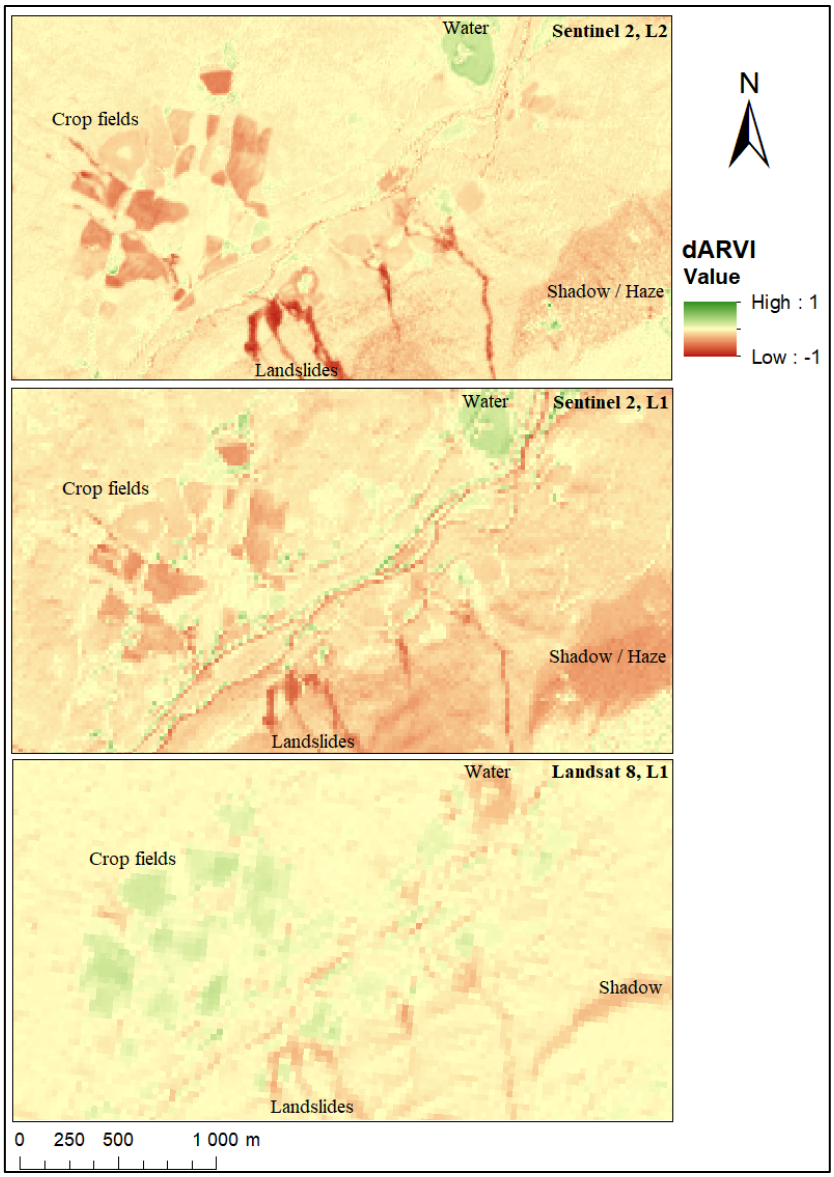

Figure 19: Displays dARVI calculated with Sentinel 2A L2, Sentinel 2A L1, and Landsat 8 L1. Different elements like crop fields, landslides, water, and shadow are marked in the maps. This enlarged section is in the western part of Jølster municipality.

6.3 Vegetation Indices - Oso

For the Oso event, both dARVI and dNDVI recognize the change in vegetation caused by the landslide in 2014. Figure 20 shows the calculation of dARVI, and figure 21 shows the calculation of dNDVI. Both figures are showing a great change in vegetation where the Oso landslide is located. However, parts of the landslide contain pixel values close to zero. As a comparison, the landslides mapped in Jølster consisted of more coherent negative values.

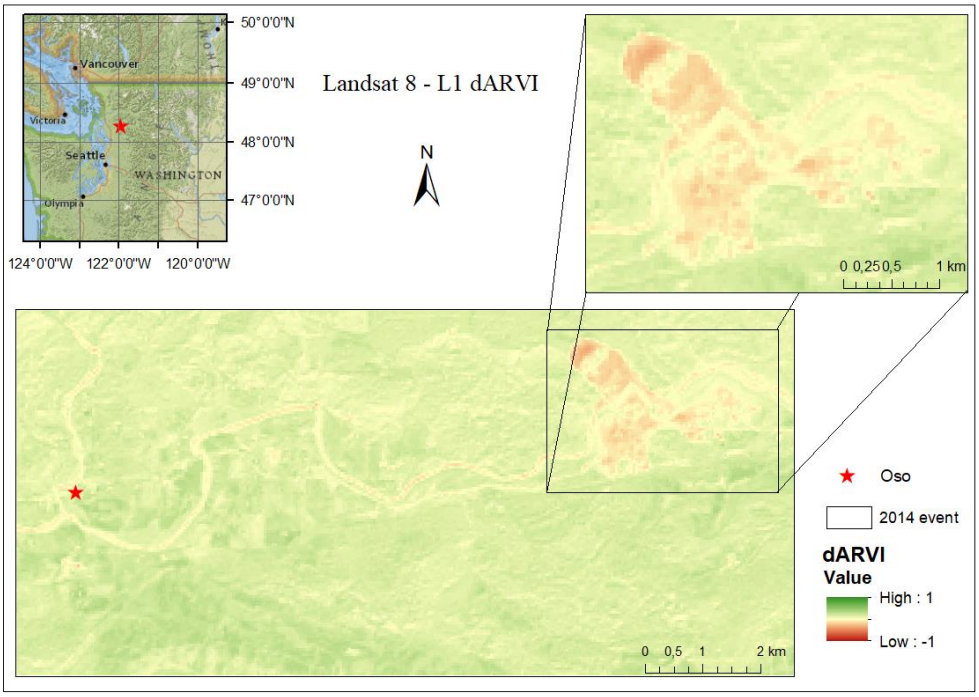

Figure 20: Calculation of dARVI with Landsat 8 data over the Oso study area in Washington. Oso is marked as a red star and the overview map in the upper left corner shows its location in Washington, USA. Southeast of Oso, an area is enlarged. This area is the site of the Oso landslide triggered in 2014. The dynamic range for dARVI is 1 to -1.

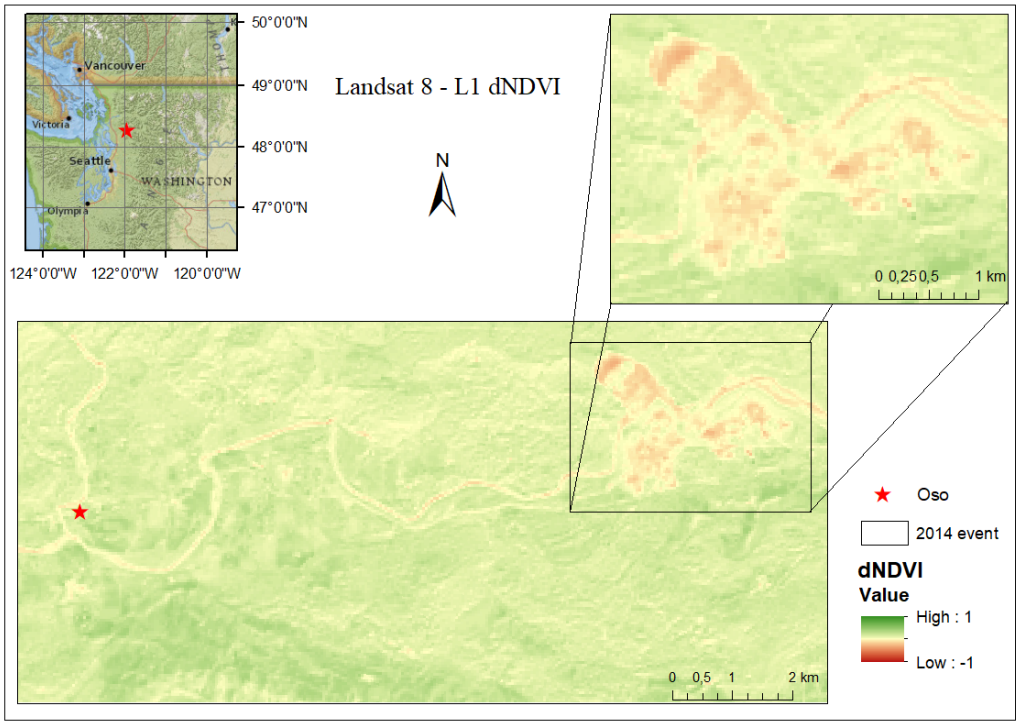

Figure 21: Calculation of dNDVI with Landsat 8 data over the Oso study area in Washington. Oso is marked as a red star and the overview map in the upper left corner shows its location in Washington, USA. Southeast of Oso, an area is enlarged. This area is the site of the Oso landslide triggered in 2014. The dynamic range for dNDVI is 1 to -1.

There is not much difference between how dARVI and dNDVI map the Oso landslide. dARVI has a slightly better coherence in negative values. The differences between the mean values of dARVI and dNDVI can be found in Table 4. Table 4 shows the mean value from both dARVI and dNDVI inside the landslide in Oso. The difference between them reveals that dARVI gives the landslide slightly more negative values than dNDVI.

Table 4: Values from both dARVI and dNDVI within the landslide polygon drawn around the landslide in Oso in 2014.

dARVIMEAN	dNDVIMEAN	Difference between dARVI and dNDVI Mean
-0.054112589	-0.042626186	-0.011486403

6.4 Additional Vegetation Indices

In addition to ARVI and NDVI, the vegetation indices GNDVI and EVI, and the water indices NDWI and LSWI, were calculated. Figure 22 displays the difference in all the six indices between the pre-and post-image, where Sentinel 2A is used as post-image. The indices are displayed over the largest landslide in Jølster municipality after the landslide event in 2019. This is the same landslide present in figure 16 and 17, located at Vassenden.

Figure 22 depicts that the greatest contrast of the landslide to the surroundings is identified using dARVI. The use of dNDVI and dEVI also highlights the landslide with great contrast to the surroundings, but yields less strong negative values. dEVI is, however, noisier than dARVI and some of the smaller landslides further north-south in the display are not detected.

Further, dGNDVI gives weaker signals to the landslides compared to the other vegetation indices but is less noisy than dEVI.

The differences in the two water indices also map the landslide with great contrast to the surroundings. dNDWI maps the landslide extent similar to the vegetation indices, while dLSWI maps the top of the landslide comparatively poor.

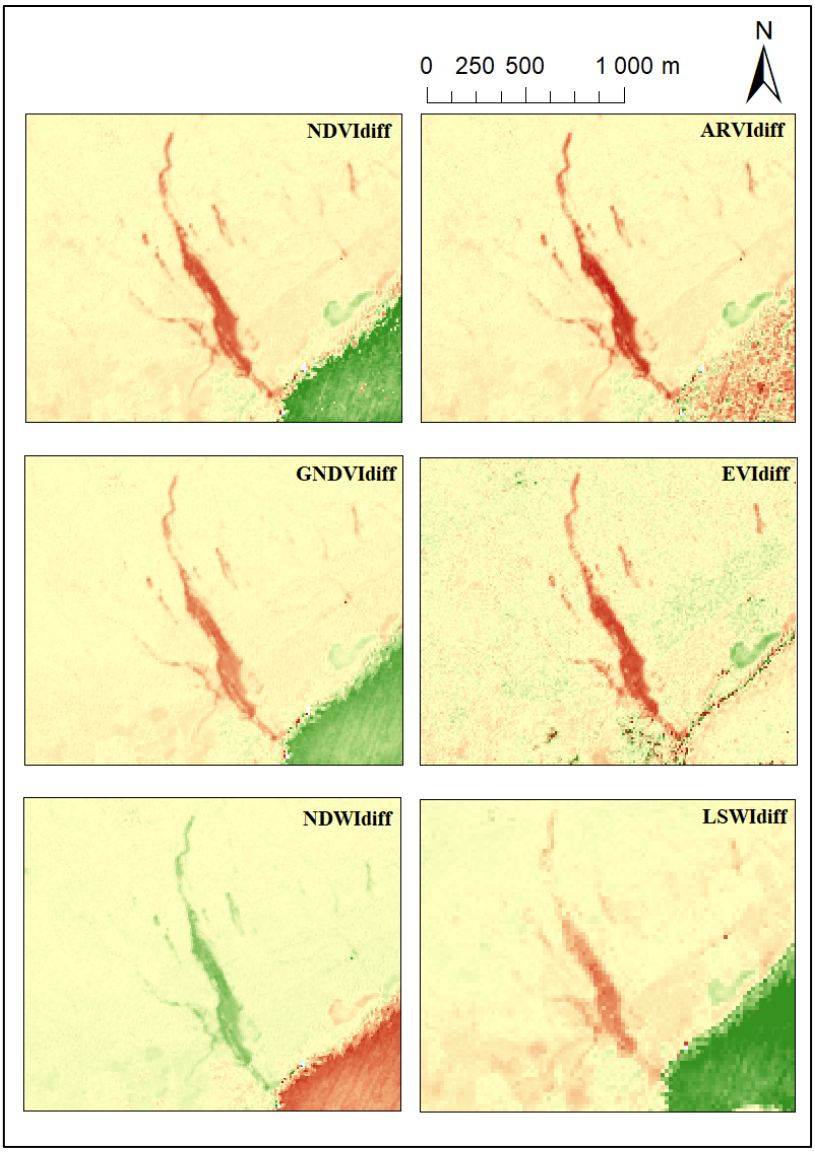

Figure 22: Overview of all the indices calculated in this study with the use of Sentinel 2 L2 data. The indices are displayed over an enlarged section of Jølster municipality above Vassenden. In this figure NDVIdiff = dNDVI.

6.5 Landslide detection – Manual Mapping

In the manual mapping approach of landslides in Jølster municipality, 108 landslides were recognized through a systematic screening of areas with clusters of negative pixel values using dARVI calculated with Sentinel 2, L2 data (Figure 23). A large portion of the identified landslides is located in the western part of Jølster municipality. The landslides varied in size. The largest landslide had an area of 92986 m^2 and the smallest had an area of 146 m^2. From literature, it is known that debris flows usually initiate at a slope between 25 and 45 (NVE, 2020b). Of the 108 Jølster landslides, 48 of the identified landslides were initiated outside this threshold. Specifically, 13 initiated over 45 degrees and 35 initiated under 25, where the highest degree a landslide initiated was 54 degrees and the lowest 9 degrees. Further, 16 of the mapped landslides had a runout beneath 5 degrees. All of these 16 landslides followed a river.

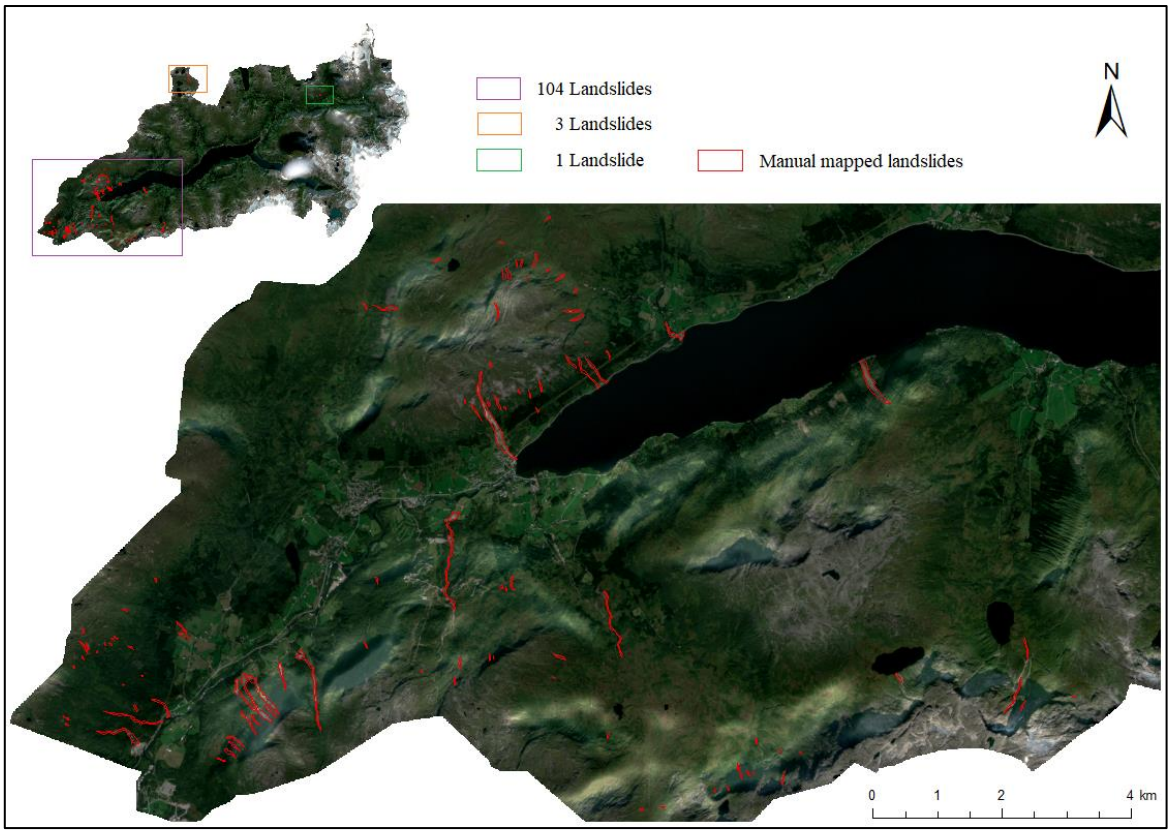

Figure 23: Landslides mapped manually using dARVI. 104 of the landslides were mapped in the western part of Jølster municipality (purple rectangle), 3 in the north (orange rectangle), and 1 further east in the project area (green rectangle). The background map is the post-image captured by Sentinel 2A.

Both dARVI and dNDVI gave strong signals in the same landslides with the same spatial extent, and the 108 landslides recognized by dARVI, were also recognized by dNDVI. Further, no additional landslides were found with dNDVI.

Through a mean value comparison of dARVI and dNDVI in the table created using "Zonal Statistics as Table" where Sentinel 2A is used as post-image, dNDVI proved to recognize 20 of the 108 landslides better than dARVI, i.e., landslides included pixels with stronger negative values inside the landslide polygons. When using Sentinel 2B as post-image, dNDVI only depicted 11 of the 108 landslides stronger than dARVI. Tables 5 and 6 contain the mean value of the 20 and 11 landslides mapped better with dNDVI than with dARVI presented as a positive difference between dARVI and dNDVI due to subtracting dNDVI from dARVI.

Table 5: Statistics derived from Zonal Statistics of the 20 cases where dNDVI was better than dARVI to map landslides in Jølster, with the use of Sentinel 2A as post-image.

Biggest difference dARVI < dNDVI			
Landslide ID (FID)	dARVI S2A Mean Value	dNDVI S2A Mean Value	Difference between dARVI and dNDVI Mean
88	-0.318118831	-0.453055978	0.134937147
96	-0.290397033	-0.354997814	0.064600781
104	-0.185787245	-0.249546448	0.063759203
2	-0.380483911	-0.421995062	0.041511151
107	-0.177801579	-0.216712564	0.038910985
97	-0.283725633	-0.315874196	0.032148563
66	-0.326210366	-0.349430587	0.023220221
95	-0.305081891	-0.328178987	0.023097096
1	-0.325742724	-0.348223237	0.022480513
8	-0.395254957	-0.416763477	0.021508519
3	-0.337241735	-0.357364623	0.020122888
90	-0.241421814	-0.261336707	0.019914893
89	-0.263699988	-0.281717374	0.018017386
87	-0.331008441	-0.34639686	0.015388419
5	-0.363296813	-0.378539365	0.015242551
98	-0.315444474	-0.330514997	0.015070523
67	-0.330002913	-0.341084489	0.011081576
105	-0.338887274	-0.344759572	0.005872298
64	-0.211513253	-0.216341755	0.004828502
65	-0.195570186	-0.198641818	0.003071632

Table 6: Statistics derived from Zonal Statistics of the 11 cases where dNDVI was better than dARVI to map landslides in Jølster, with the use of Sentinel 2B as post-image.

Biggest difference dARVI < dNDVI			
Landslide ID	dARVI S2B MEAN	dNDVI S2B MEAN	Difference between dARVI and dNDVI Mean
105	-0.158786938	-0.198765971	0.039979033
2	-0.2576706	-0.283302684	0.025632084
1	-0.210704938	-0.226337996	0.015633058
8	-0.191821362	-0.206232092	0.01441073
89	-0.200269635	-0.20810752	0.007837885
54	-0.050291398	-0.053245144	0.002953746
59	-0.044929653	-0.047552489	0.002622835
39	-0.005721006	-0.007570085	0.001849078
82	-0.09016958	-0.091556689	0.001387109
51	-0.022610463	-0.023290746	0.000680283
33	-0.014532843	-0.015084156	0.000551313

Moreover, even if the landslides were better recognized by dNDVI in respectively 20 cases for Sentinel 2A, and 11 cases for Sentinel 2B, table 5 and 6 reveals that the difference between dNDVI and dARVI is not significant. An overview of the 20 and 11 scenarios where dARVI performed relatively best is given in table 7 and 8. Here the difference is greater.

Table 7: Statistics derived from Zonal Statistics of the 20 best cases where dARVI was better than dNDVI to map landslides in Jølster, with the use of Sentinel 2A as post-image.

Biggest difference dARVI > dNDVI			
Landslide ID (FID)	dARVI S2A Mean Value	dNDVI S2A Mean Value	Difference between dARVI and dNDVI Mean
45	-0.596975244	-0.500293832	-0.096681411
31	-0.621111333	-0.529415827	-0.091695506
61	-0.428651048	-0.353990283	-0.074660765
48	-0.413069793	-0.344401105	-0.068668688
10	-0.534074489	-0.469934033	-0.064140456
78	-0.275342107	-0.212606569	-0.062735538
30	-0.329943249	-0.269133286	-0.060809963
92	-0.353265944	-0.293051243	-0.060214701
35	-0.440574106	-0.382261896	-0.05831221
57	-0.35285972	-0.295779494	-0.057080226
85	-0.293526018	-0.236952105	-0.056573913
56	-0.4658379	-0.409462189	-0.056375711
55	-0.456335365	-0.400675868	-0.055659497
106	-0.325011916	-0.272485465	-0.052526452
11	-0.25942634	-0.208836764	-0.050589576
9	-0.573814439	-0.524643911	-0.049170528
20	-0.302371874	-0.253512502	-0.048859373
12	-0.435743367	-0.39002545	-0.045717917
68	-0.299848393	-0.25519295	-0.044655442
86	-0.252479144	-0.208237706	-0.044241438

Table 8: Statistics derived from Zonal Statistics of the 11 best cases where dARVI was better than dNDVI to map landslides in Jølster, with the use of Sentinel 2B as post-image.

Biggest difference dARVI > dNDVI			
Landslide ID	dARVI S2B MEAN	dNDVI S2B MEAN	Difference between dARVI and dNDVI Mean
45	-0.566687052	-0.469302645	-0.097384406
31	-0.561481519	-0.476654206	-0.084827313
9	-0.523001382	-0.456555969	-0.066445414
7	-0.537264222	-0.475267192	-0.06199703
93	-0.343169848	-0.285593996	-0.057575852
92	-0.308934373	-0.251370886	-0.057563487
61	-0.359680036	-0.302720764	-0.056959272
10	-0.444209446	-0.390447957	-0.053761489
86	-0.265367636	-0.213319941	-0.052047694
106	-0.293837003	-0.244210392	-0.049626611
56	-0.380999038	-0.334117533	-0.046881505

Further, 43 of the 108 Jølster landslides were recognized with Landsat 8 data (Figure 24). The spatial extent of the 43 landslides identified by Landsat 8 had in most cases a smaller area than those recognized by Sentinel 2. Figure 24 displays manual mapped landslides, by both Landsat 8 (blue color) and Sentinel 2 (red color). In most cases, landslides with the greatest area were recognized by Landsat 8, but the smaller landslides were not. Even if Landsat 8 did not suffer from cloud cover, no additional landslides were recognized. Landsat 8 only recognized landslides in the western part of the municipality.

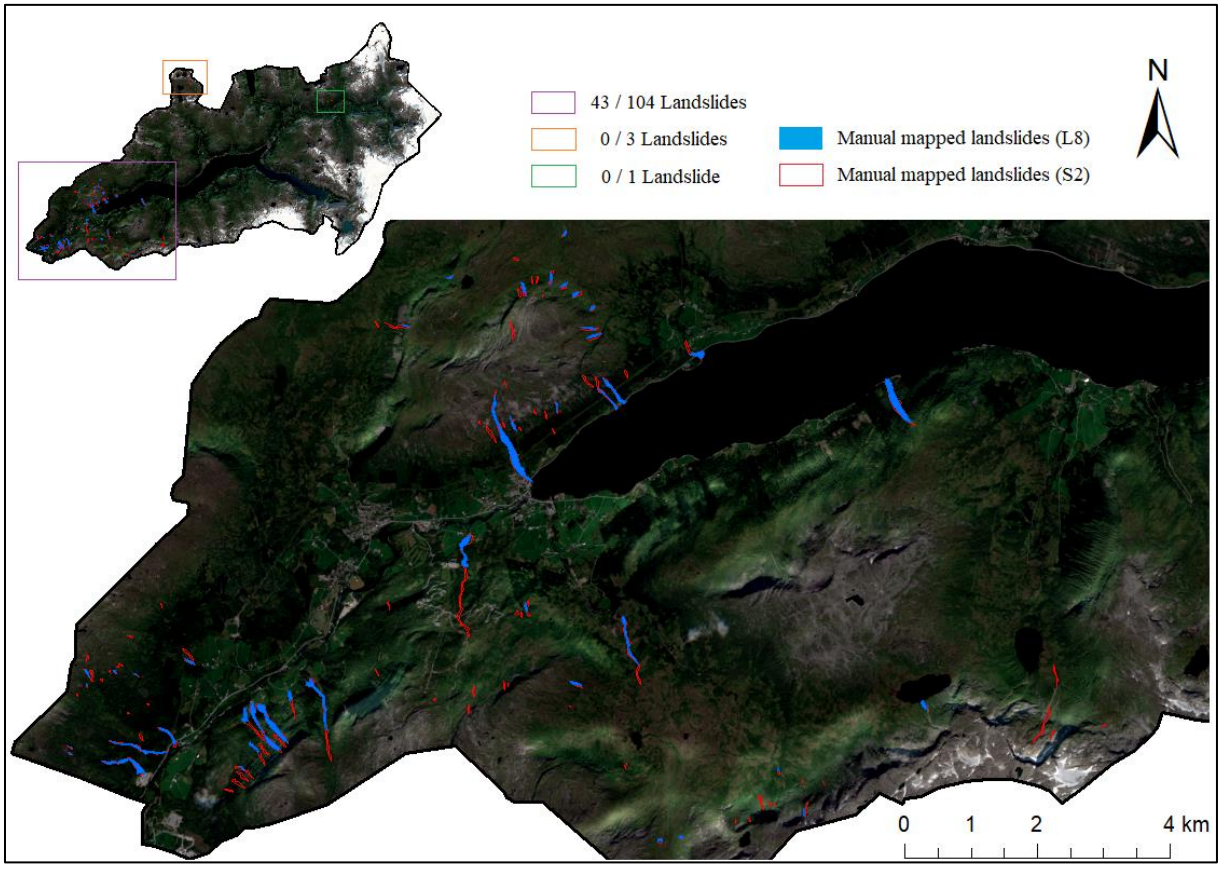

Figure 24: Display of both landslides manual mapped with Sentinel 2 data and Landsat 8 data. All of the landslides recognized by using dARVI calculated with Landsat 8 data were mapped in the western part of Jølster, with no recognition of landslide elsewhere in the project area. In the upper left corner of the figure, there are drawn three rectangles in Jølster municipality, and a comparison between how many landslides are registered by Landsat 8 data vs Sentinel 2 data is given.

Further, figure 25 shows the mapping result from both Sentinel 2 and Landsat 8 together with the landslides registered in the NVEs landslide database, marked as yellow stars. All of the 18 landslides present in the NVEs landslide database were detected in this study with the use of Sentinel 2 data. 13 of the 18 landslides in the existing database were detected by Landsat 8 data.

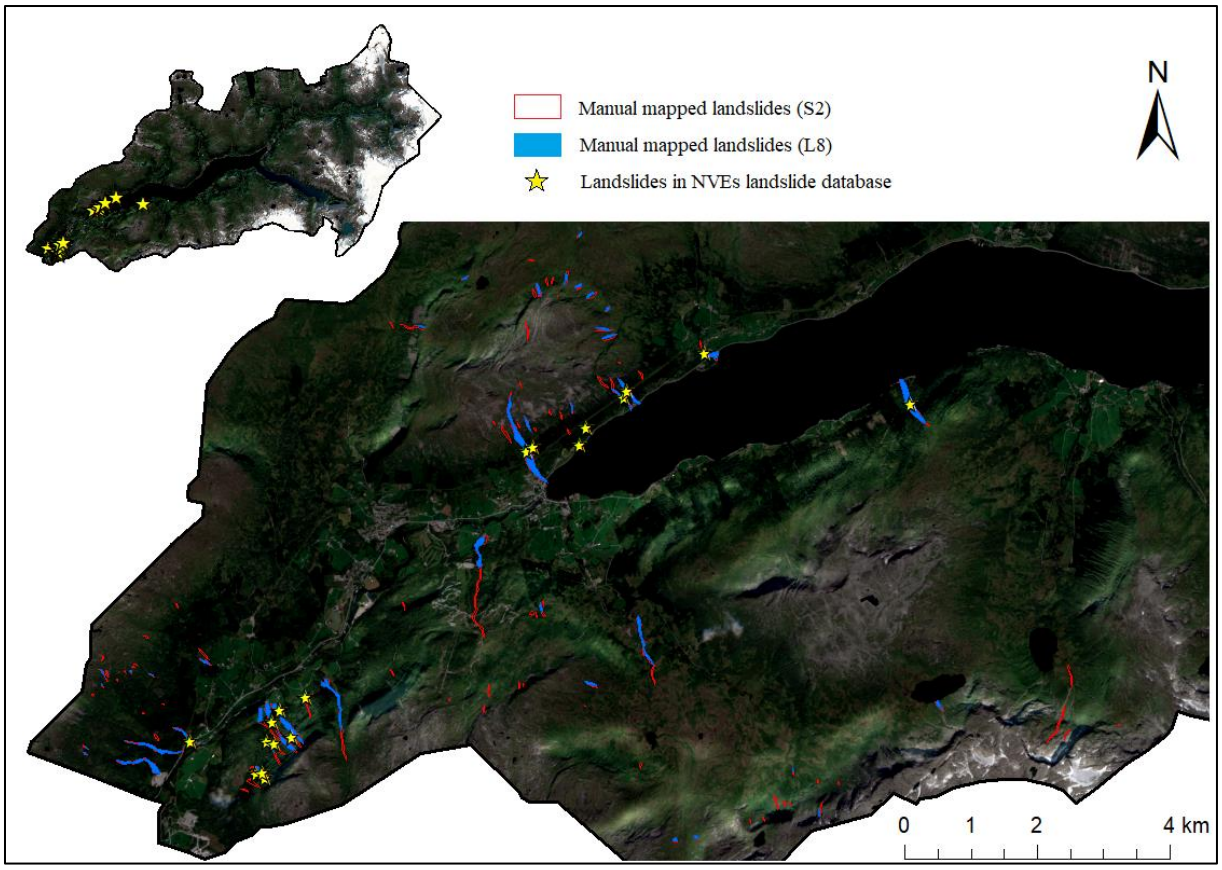

Figure 25: Displays landslides mapped with the use of both Sentinel 2 and Landsat 8, in addition to the location of landslides in NVEs existing landslide database.

6.6 Landslide detection in Raster Calculator

The equations used in Raster Calculator are introduced in the method chapter 5.3.2. In Equation 1, dARVI values as the difference between Sentinel 2A pre- and post-image is used. With this equation, 51 of the 108 Jølster landslides were recognized with at least one pixel (Figure 26). Respectively, 56 of the 108 Jølster landslides were recognized with the use of Equation 2 which includes dARVI values as the difference between Sentinel 2A pre-image and Sentinel 2B post-image (Figure 27). In the results of both equations, only a few pixels inside the landslide polygon were detected.

In figure 26 and 27, the results from the two equations used in Raster Calculator is displayed in the western part of Jølster municipality. Several pixels in the result are located outside the mapped landslide polygons. In figure 26 these pixels represented elements such as haze, crop fields, and rivers. In figure 27, the pixels outside the landslide polygons represent rivers. In most cases, Equation 2 maps landslides more precisely than Equation 1 by mapping more of the landslides and less of other false positive elements. Neither of the two equations detected additional landslides to the landslides that were mapped manually.

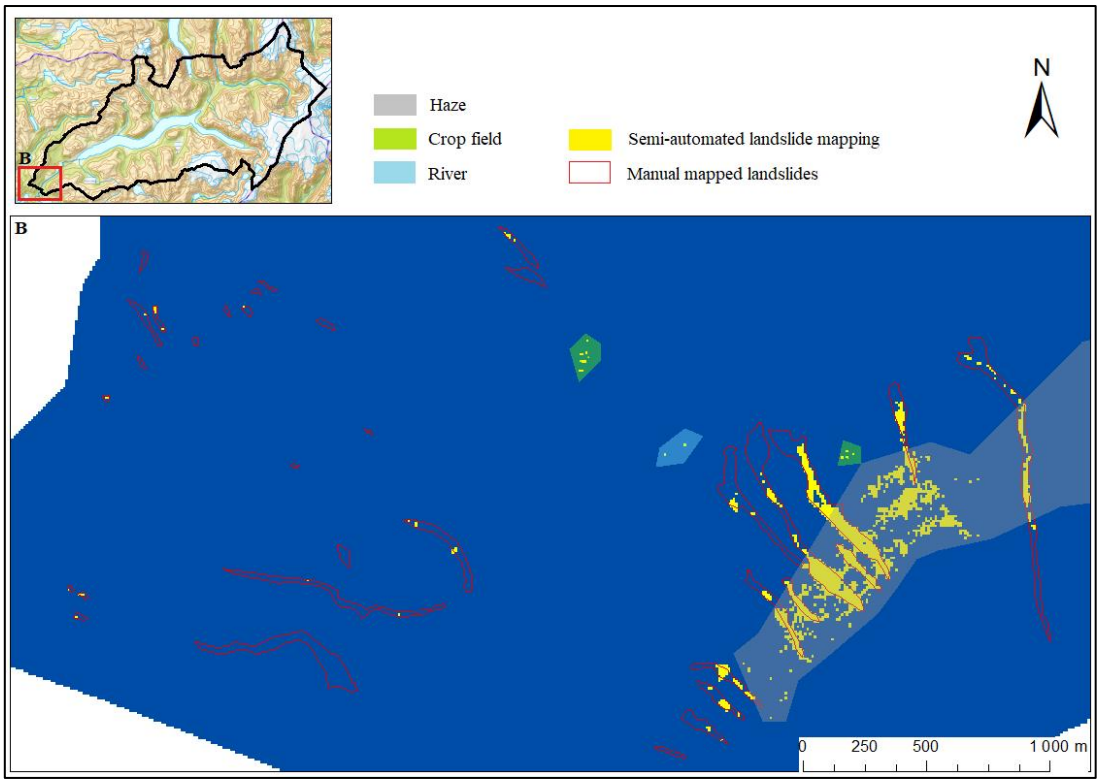

Figure 26: The results from the landslide mapping in the Raster Calculator using Equation 1. Pixels represented in yellow indicate those areas which were true for the equation. The pixel outside a landslide polygon is classified as either haze, crop field, or river.

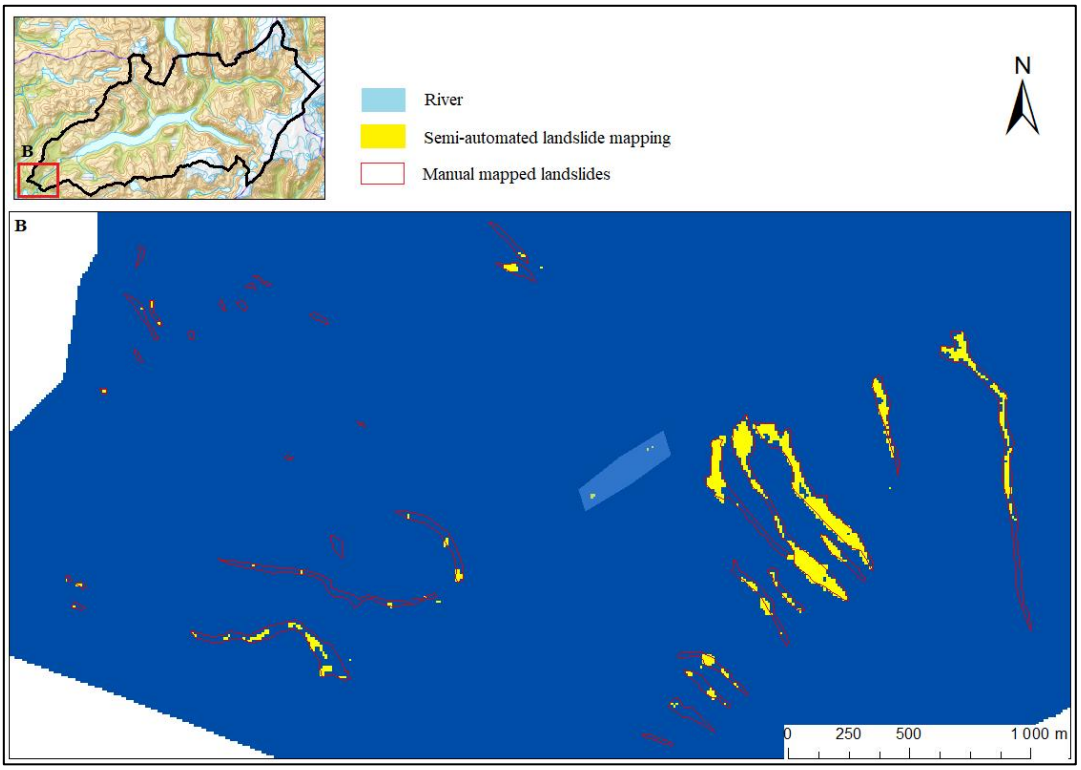

Figure 27: The result from the landslide mapping in the Raster Calculator using Equation 2. Pixels represented in yellow indicate those areas which were true for the equation. The pixel outside a landslide polygon is classified as a river.

7 Discussion

This section will discuss and interpret the results, including the validity of the results and methods used. The discussion section will be organized as follows: First, topics concerning data collection and visualization, including locations analyzed, methods used for data collection and processing, and visualization techniques. Second, the methodologies used for analyzing the data to map landslides. Third, difficulties are associated with comparing the results and findings of this study with the ongoing Ph.D. research by Lindsay (Ph.D. candidate, NTNU).

7.1 Data collection and visualization

7.1.1 Study areas

The two study areas chosen for this study have similar climatic challenges. Both Jølster municipality located in the western part of Norway and Oso located in Washington, USA have humid climates which are highly affected by clouds, air humidity, and high precipitation amounts. These are factors that influence optical satellite data, and may potentially impact the validity and reliability of the results (SafeLand D4.5, 2011). The high presence of dense vegetation at both case sites facilitates the use of vegetation indices, and the topography is well suited for the use of optical satellite data.

The atmospheric resistant vegetation index ARVI may superior to the widely used vegetation index NDVI under these conditions, and to assess this both indices were used in the analyses and results compared. However, if the study areas had less vegetation, the approach would be limited due to results of NDVI is better in areas with a great presence of dense vegetation (Guzzetti et al., 2012), and the improvement of ARVI is much better for vegetated surfaces than for soil (Kaufman & Tanre, 1992).

A key difference between the Jølster and Oso events is the nature of the occurrence of the landslides. At Jølster numerous landslides occurred during (following) a single period of heavy precipitation, whereas at Oso only one landslide occurred during the recent precipitation event. However, at Oso, there is evidence of several historical landslide events. The Oso event was known and well documented (Aaron et al., 2017; Stark et al., 2017; Wartman et al., 2016), whereas at Jølster only a small number of the landslides were identified and registered in the NVEs landslide database: 18 of a total of 108 landslides were registered in the database (Devoli, 2021). No further mapping was therefore undertaken at the Oso case site. This case site was used to evaluate the replicability of the method.

7.1.2 Data collection and pre-processing

Optical satellite data were retrieved for this study, and the optical data used consisted of images from the Sentinel 2 mission and the Landsat 8 mission.

A cluster of landslides is more difficult to separate with the use of optical data, hence limiting the reliability of mapping the correct number of landslides (Hölbling et al., 2015). If several landslides are triggered at the same location, optical satellite data would treat this as only one. The landslides mapped at both case sites using optical satellite data only presents changes due to the specific events and contains no additional information caused by previous landslides.

Radar data was considered, however, the topography in Jølster limits the use of radar approaches described in e.g., Yang et al. (2019). Lindsay (2021) also argues that the use of optical satellite data is more appropriate than the use of radar for the Jølster case site. In Lindsay's Ph.D. study, 120 landslides were identified using Sentinel 2 data, only 9 landslides were mapped with the use of Sentinel 1 data (Lindsay, 2021). Previous studies on the Oso site have used LiDAR and InSAR techniques which enables distinguishing between old and new landslides at the same site (Stark et al., 2017; Sun et al., 2015). Methods based on radar imaging are suitable for Oso but are of limited use in Jølster.

Two factors are important when choosing optical satellite images to use for change detection: timing of the images in relation to the landslide event of interest, and the presence of cloud cover in an individual image. Optimally images are selected just before, and just after the event for the highest fidelity in the landslide imaging (Hölbling et al., 2015). However, problems with cloud cover in the images may limit the usability of the most optimal images (Mill et al., 2014). Complicating this is the differing acquisition schedules for the two platforms. For Jølster, the Sentinel 2 constellation provides both Sentinel 2A pre- and post-image and Sentinel 2B post-image data sets. The post-image retrieved from Sentinel 2A had a bigger time gap between the landslide event and when the image was taken compared to the post-image collected by Sentinel 2B. Sentinel 2A post-image was taken 29 days after the event while the Sentinel 2B post-image was taken only 3 days after the event.

Landslide scars may diminish over time due to different factors that the landslide masses are exposed to (Behling et al., 2016). Moreover, seasonal changes may also affect the land cover features and cause unwanted changes like a difference in vegetation and snow- and ice conditions. Furthermore, these changes affect the corresponding spectral features in the optical

satellite data (Tehrani et al., 2021). Choosing post-images several months after a landslide event can result in landslides not being detected.

Where a cloud is present in an optical satellite image, some form of cloud removal process is necessary before the underlying terrain can be analyzed for landslide detection (Mill et al., 2014). The Landsat 8 images collected for this study had no cloud cover, in addition to the Sentinel 2 pre-image. However, both the Sentinel 2 post-images were affected by clouds. Removal of clouds is often one of the first things to do in the image processing (Gómez-Chova et al., 2017), but with the use of two post-images, the manual mapping had to be done in a two-step process, which allowed for a manual search in the entire areas without primary cloud-removal. The cloud removal was therefore performed prior to the semi-automatic mapping approach in the Raster calculator.

The Sentinel 2A post-image was affected by two bigger clouds, while the Sentinel 2B post-image was affected several places by smaller clouds. This difference in cloud cover complicated the removal of clouds, and two different cloud-removal processes had to be applied to the Sentinel 2 post-images.

The clouds present in the Sentinel 2A post-image were removed using Pixel editor in ArcGIS Pro. This approach relies on available cloud-free images which can be challenging to collect. Moreover, the cloud-free image should be as close as possible in time taken due to the effect of sessional differences. This cloud-removal process with the use of Pixel Editor in ArcGIS Pro would have been much more time-consuming with the Sentinel 2B post-image as several more areas would have to be replaced.

Further, the clouds present in the Sentinel 2B post-image were removed using the Raster calculator. Band 2, gave the biggest contrast for clouds relative to the surroundings and was selected for analysis over the other bands. The use of band 2 is also recommended by Bréon and Colzy (1999). This approach relies on the clouds having a distinct change in pixel values compared to other elements. The density of the clouds in the Sentinel 2A post-image varied, and especially near the edges, the cloud were thin and transparent. The pixel values in these areas were similar to those representing landslides. By applying the approach of cloud removal in Raster Calculator to the Sentinel 2A post-image, either too much information not concerning clouds was excluded, or pixels representing cloud were still present. Removing clouds in the Sentinel 2A post-image in Raster Calculator without compromising landslide information was therefore not possible.

Due to the difference in time between the two Sentinel 2 post-images and the difference in cloud cover, it was necessary to include both post-images for a more precise landslide mapping. Timing supported the use of the Sentinel 2B post-image, taken only 3 days after the Jølster event. In fact, dARVI calculated with the use of Sentinel 2B post-image yields stronger negative pixel values to the landslides compared to the pixel values in dARVI calculated with the use of Sentinel 2A post-image. This may be a consequence of the difference in the time the post-event satellite images were taken, and supports the statement in Tehrani et al. (2021) that time can affect the spectral features. However, the Sentinel 2A post-image was less affected by clouds, which supported the use of the Sentinel 2A post-image.

7.1.3 Vegetation indices and Water indices

In this study, the vegetation indices NDVI, ARVI, EVI, and GNDVI, were calculated. In addition to two water indices GNDWI and LSWI. Further, the difference between the indices calculated for two images separated by time was compared. E.g. dNDVI = NDVI post-image – NDVI pre-image. This was done to see how the different indices corresponded to the total change from before and after the landslide events. This bi-temporal approach is widely used for post-failure mapping (Cheng et al., 2004; Lacroix et al., 2013).

NDVI is the most commonly used vegetation index in landslide mapping (Bannari et al., 1995). This vegetation index was utilized by Ph.D. candidate Erin Lindsay, and for comparison, it was chosen for this study as well. NDVI is in addition often used as a reference to evaluate other indices (Bannari et al., 1995), and in this study, it is used to evaluate especially the vegetation index dARVI. With the use of dNDVI all the 108 landslides detected in this study were highlighted as elongated clusters of pixels with negative values.

ARVI is another index with high potential in this setting, which corrects NDVI for atmospheric effects (Kaufman & Tanre, 1992). dARVI was the index that gave landslides the lowest negative pixel values, independent of which satellite images were used, and thereby giving landslides pixel values with great contrast to the surroundings. dARVI was therefore chosen to be used in both the manual mapping and the semi-automatic mapping approach in the Raster calculator.

The calculation of ARVI is more demanding than for NDVI. With the use of ARVI, location plays an important role due to different types of aerosols which have to be taken into consideration when calculating this index. Choosing an appropriate y-value in the ARVI equation is crucial for the result as explained by Kaufman and Tanre (1992). They argue that

the y-value of 1 gives the best results in most RS applications. Supporting Kaufman and Tanre (1992), the value of 1 has proven to be the optimum value, giving the best result. For comparison, y-values of both 0.5 and 2 were tried, where the use of both values underestimated the changes caused by landslides.

Moreover, ARVI was created for MODIS, and band 8A was therefore tested in the formula instead of band 8 because 8A has a closer spectral location to band 8 for MODIS. The result from using band 8A gave landslide-affected areas a less distinct contrast to the surroundings, in addition, the spatial extent of these areas was smaller due to more pixels with values closer to zero. The resolution of the bands differs where band 8A has a resolution of 20 meters while Band 8 has a 10-meter resolution. In other studies combining Sentinel 2 and ARVI, band 8 is used (Kobayashi et al., 2020).

From the results, it is proven that the vegetation index dEVI also highlights landslides with great contrast to the surroundings. However, it is important to notice that dEVI is noisier than dARVI and does not map smaller landslides as well as dARVI and dNDVI. Several of the landslides mapped in Jølster municipality, linked to the event on 30th of July 2019, had small areas, and the use of dEVI in further landslide mapping could have excluded several landslides. Moreover, the fact that dEVI gives landslides lower negative values than dNDVI, supports the idea that atmospheric resistance improves the landslide detection in humid climates, but only for landslides of a certain size. For this study, it was not necessary to use two vegetation indices that correct NDVI for the same elements, in this case, atmospheric effects (Matsushita et al., 2007).

Hölbling et al. (2015) argue that GNDVI can improve the detection of landslides with smaller areas, not captured by NDVI. This study does not support this statement when the results did not reveal that the use of dGNDVI mapped landslides with smaller areas better than dNDVI. Especially not with the use of L2 data which was utilized in the mapping process. Further, dGNDVI did neither map smaller landslides better than dARVI.

Both water indices calculated highlighted rivers and water, also rivers where landslides were mapped in addition to landslides not following rivers. This was expected due to the water content of landslides triggered as a consequence of heavy rainfall events. dNDWI highlighted these objects slightly better than dLSWI. This may be due to both bands in the calculation of dNDWI having a 10-meter resolution, while the SWIR band used in the calculation of dLSWI has a 20-meter resolution. The water indices were neither utilized in the manual mapping when

the difference between rivers with and without soil accumulation was similar. Further, dNDWI was utilized in the semi-automated landslide mapping in Raster Calculator since rivers were some of the objects that had to be excluded.

In summary, dARVI and dNDVI gave better results in recognizing landslides by giving pixel values that represented landslides, a greater contrast to the surroundings, independent of size. The other indices calculated in this study were therefore not utilized.

The dARVI and dNDVI highlighted the same number of landslides in Jølster municipality and both showed a significant change in vegetation at the Oso case site as well. However, the results indicate that dARVI maps better than dNDVI, revealed by the mean pixel values inside the landslide polygons. This was true in all except 20 landslides mapped in Jølster linked to the Jølster event in 2019, with the use of Sentinel 2A post-image, and 11 landslides mapped in Jølster with the use of Sentinel 2B post-image.

The tables in the result listing the 20 and 11 landslides mapped better with dNDVI reveals that even if these landslides gained a stronger negative pixel value with the use of dNDVI, the difference in how dARVI mapped these landslides was minimal. In fact, by looking at the tables listing the 20 and 11 landslides mapped best with the use of dARVI, the difference is bigger.

Further, by comparing the 20 landslides and 11 landslides that were mapped best with dNDVI, only 5 of these are present in both cases. This means that 15 of the 20 landslides mapped best with dNDVI with the use of Sentinel 2A post-image were mapped best with dARVI with the use of Sentinel 2B post-image. Respectively, 6 of the 11 landslides mapped best with dNDVI with the use of Sentinel 2B were mapped best with dARVI with the use of Sentinel 2A.

It was challenging to find an explanatory factor for why some of the landslides were mapped better with the use of dNDVI. For the 11 landslides, it seems like dNDVI mapped landslides better than dARVI if the mean values were closer to zero. This discovery is more diffuse for the 20 landslides where the mean values are more negative.

Further, for finding explanatory factors for why dNDVI mapped landslides better in some cases, the attribute table for the manually mapped landslides was used. For instance, the 20 landslides mapped best with the use of dNDVI calculated with the Sentinel 2A post-image, had an area under 7000 m^2. The mean area of all the 108 landslides was 8090 m^2 and it was tested to see if dNDVI mainly mapped smaller landslides better than dARVI. Out of all the 108 landslides, mapped manually in this study, 89 landslides had an area under 7000 m^2. Out of the 89

landslides, only 20 mapped better with dNDVI than dARVI revealing that there are no combinations with dNDVI mapping landslides under a certain area better than dARVI. The same observation was made for the 11 landslides mapped better with dNDVI calculated with the Sentinel 2B post-image. Further, there was neither a combination between these landslides mapped best with dNDVI and initiating slope, runout, or that they followed a river.

It is argued that ARVI is four times less sensitive to atmospheric effects than NDVI (Kaufman & Tanre, 1992). This improvement of resistance to atmospheric effects may be the reason for the better results with the use of dARVI compared to dNDVI.

7.2 Landslide Mapping

Due to the moderate resolution of the optical satellite data retrieved for this study, an object-based method for mapping landslides is not used. Several of the landslides detected in this study are only a few pixels wide, at least in one dimension. This does not lead to well-defined objects.

Two types of methods for mapping landslides were tested. First, a manual landslide mapping method, and secondly, a semi-automatic method. The results from these landslide mapping approaches reveal that the results are highly influenced by the different types of data and the approaches used to identify landslides.

7.2.1 Manual mapping

The manual mapping was performed for getting an overview of how many landslides the different data collected for this study, contributed with finding. During the manual mapping, it was discovered whether two satellite sensors with different resolutions detected the same landslides, how L1 data recognize landslides compared to L2 data, and which vegetation indices contributed the best with detecting landslides.

The manual mapping with the use of Sentinel 2 data was conducted in a two-step process including images from both Sentinel 2A and Sentinel 2B. The entire study area was then searched two times for mapping the landslides. This was necessary to overcome the presence of clouds in the Sentinel 2 post-images. This two-step process, however, resulted in an increasingly complex manual interference in the data, hence weakening the process efficiency.

The manual mapping with the use of Landsat 8 data was done by comparing the landslides mapped by the Sentinel 2 data and further study where elongated clusters of negative pixel values were present in the Landsat 8 image.

Both Sentinel 2 and Landsat 8 contributed to identifying a significantly greater number of landslides inside Jølster municipality, caused by the Jølster event in 2019, than the number of landslides registered in NVEs landslide database. From before, only 18 landslides were registered in the landslide database linked to the Jølster event in 2019 (Devoli, 2021). The Sentinel 2 data recognized these 18 landslides in addition to 90 landslides, whereas Landsat 8 detected 13 of the 18 landslides and contributing to finding 30 additional landslides.

In the manual mapping, the use of the Sentinel 2 data resulted in identifying 65 more landslides than the Landsat 8 data. Moreover, in many cases, Landsat 8 only mapped parts of the landslides detected by the Sentinel 2 data. One explanation for this can be due to the coarser resolution of Landsat 8. In previous research, Landsat 8 is described as more suitable for regional mapping and has difficulties recognizing smaller landslides, specifically less than a few hundred square meters (SafeLand D4.4, 2011). In this study, landslides with small areas were not identified when using Landsat 8 data.

Further, only L1 data was retrieved for Landsat 8. The comparison between Landsat 8 L1, Sentinel 2 L1, and Sentinel 2 L2 data in the result indicated that smaller landslides were harder to detect with L1 data. Moreover, there was a significant difference between L1 and L2 in how great the landslides contrast were to the surroundings. Both in dARVI and dNDVI, L1 data revealed a weaker negative pixel value for landslides than L2 data. The search for landslides was based on elongated clusters of pixels with negative values with the use of dARVI and dNDVI. Due to this, there may have been landslides with more diffuse pixel values which were not detected. The combination of coarser resolution for the Landsat 8 data in addition to only retrieving L1 data for Landsat 8 may be the reason for the different amount of landslides detected with the two satellite sensors.

However, the total number of landslides detected with the Sentinel 2 data may be wrong. Several of the smaller landslides detected with Sentinel 2 data, had their location in an area of dense forest. These small landslides can potentially be a part of a larger landslide or be changes caused by deforestation. Further, there may also be smaller landslides not detected with Sentinel 2 data. Previous research has found that Sentinel 2 is unable to detect landslides smaller than 100 m^2 (Yang et al., 2019). This study was unable to identify any landslides beneath 146 m^2, thus supporting the previous findings.

Moreover, shadows were present along most hillsides. In these areas, interpreting landslides with certainty proved to be a difficult task due to similar pixel values for shadows and

landslides. Fiorucci et al. (2019) argue that the use of NDVI can improve landslide mapping in shadow-affected areas. In this study, dNDVI did not provide a more accurate result in the mapping of landslides in shadow-affected areas compared to dARVI. In addition, with the use of the Sentinel 2A post-image, these areas were often influenced by haze. The presence of haze may counteract the dNDVI performance of detecting landslides in areas with shadows due to larger areas covered by negative pixel values. Potential landslides in shadow-affected areas were not detected in this study.

7.2.2 Landslide mapping in Raster calculator

Two equations were implemented in the Raster Calculator to detect landslides in Jølster municipality linked to the Jølster landslide event in 2019.

The final equations used in Raster Calculator was as follows:

- Equation 1; "(S2A_dARVI < - 0.2) & (Slope < 54.25) & (Slope > 15) & (DTM10m < 1336) & (Band 2 > 500) & (dNDWI > 0.3)"
- Equation 2; "(S2B_dARVI < - 0.2) & (Slope < 54.25) & (DTM10m < 1336) & (Band 2 > 500) & (Band 2 < 3000) & (dNDWI > 0.3)"

In the final result, Equation 2 mapped 5 landslides more than Equation 1. Equation 1 recognized a total of 51 landslides, and Equation 2 recognized a total of 56 landslides.

In Raster Calculator, the mapping was based on values from the manual mapping. Choosing a pixel value for the dARVI representing landslides was difficult due to other elements with similar values. No values were unique for only landslides. Inside the landslide polygons, the values varied as well, and not every pixel inside the polygons had a strong negative value. dARVI calculated with Sentinel 2 L2 data, mapped landslides the best in most cases, due to a bigger contrast to the surroundings. It was therefore decided that values from this index were to be used in the calculation in Raster Calculator.

The value of -0.2 was chosen to be used in both the calculation, excluding every pixel with a value greater than this. With the use of -0.2 in Equation 1, a total of 5 landslides was fully excluded due to having a min value greater than -0.2. Respectively, 103 landslides were ensured getting mapped with at least one pixel dimension. With the use of -0.2 as dARVI pixel value in Equation 2, a total of 17 landslides was fully excluded by having a min value greater than this. Further, 91 landslides were ensured to get mapped with at least one pixel dimension. This information is extracted from the Excel table created by the results of "Zonal Statistics as

Table". Moreover, the results reveal that even if the dARVI pixel value of -0.2 excludes more landslides in Equation 2 than in Equation 1, Equation 2 maps more landslides in addition to mapping the landslides with a greater pixel dimension. This may be due to stronger negative pixel values with the use of the Sentinel 2B post-image, in addition to other exclusions in the equation.

The values inside the landslide polygons highly depended on the area in which there is great uncertainty, especially due to the difficulty of placing the initiating point. 68 out of 108 landslides followed rivers. Only the part of the rivers where soil accumulation was visible, was mapped as a landslide. The initiating point may likely have been further up in the river, and due to this, it is likely that the area is greater than presumed. An example is that 24 out of the 68 landslides that followed a river, had a slope max beneath 25 degrees, and debris flows usually initiate above this slope (NVE, 2020b).

Further in the equation, slope and elevation were used to exclude areas not representative of landslides. The uncertainty of the initiating point influences this and limits the reliability of slope and elevation the landslides occurred at. The max slope and elevation values used in the equations may have excluded landslides, and for instance, landslides could have been present in the higher terrain.

Band 2 was applied to both the equations for excluding shadow-affected areas. This band is used, as it gives the largest contrast between shadow-affected areas and other elements present in the scene. The shadow-affected areas had similar values in both post-images and the same value was therefore applied to both equations.

Areas affected by haze were also present in the Sentinel 2A post-images. The exclusion by applying band 2 reduced the haze as well, but haze was still an element present in the result, true for the equation, but not related to landslides. Haze is a common factor influencing optical satellite images and is often hard to discover due to its transparency (Makarau et al., 2014). Several approaches have been developed to remove haze, where most of them rely on haze-free images (Makarau et al., 2014), similar to the approach for cloud detection in ArcGIS Pro with the use of Pixel Editor. With the Sentinel 2B post-image available, some of the areas where haze was present could have been removed. However, the Sentinel 2B post-image was influenced by clouds in several places where haze was present in the Sentinel 2A post-image and it was decided not to remove the haze, due to the haze present in the same area as landslides.

This negatively affected the results of Equation 1, by having false-positive pixels present in the result as a consequence of haze.

Moreover, the water index dNDWI was used to separate rivers from landslides. The difference between rivers with and without soil accumulation was similar with the use of both post-images, and a value of 0.3 was therefore used in both equations. The value of 0.3 was chosen when greater and lower pixel values either excluded rivers where landslides were present or included rivers where landslides were not present.

However, some parts of rivers without soil accumulation, not registered as landslides, were still detected by both Equation 1 and Equation 2 in Raster Calculator. Rivers were the only elements mapped other than landslides with Equation 2. For the manual mapping only those parts of rivers showing accumulation in soil, in the RGB image, were mapped as landslides. This excluded other changes, for example, changes caused by greater water flow, which also is a consequence of periods of heavy rain and precipitation. Several parts of rivers mapped by Raster Calculator did not show evidence of soil accumulation, and the change is most likely due to higher water flow. The higher water flow in the rivers highlighted in the results of the Raster Calculator with the use of Equation 1, does not necessarily have anything to do with the event of interest, due to the 30 days' time delay.

Two parts of the equations differ from one another. This is due to the removal of crop fields and the removal of clouds. Crop fields were some of the features remaining in the result with the use of Equation 1. With the use of the Sentinel 2A pre- and post-image, crop fields were given negative values, close to those representing landslides. Since the Sentinel 2A post-image was retrieved 30 days after the event, in the middle of the summer, the reason for negative values on crop fields may be due to harvesting. Harvesting is a common problem in detecting landslides in populated areas, and an approach to reducing the effects of crop fields is to remove urban areas where they are present. This is done in Mondini et al. (2011). A limitation due to this approach is that no landslide will be detected in such areas.

Moreover, separating the crop fields from landslides in this study, all areas with a slope less than 15 degrees were excluded in Equation 1 to remove crop fields. This lead to 39 of the landslides being at least partially excluded. The partially excluded landslides had a runout beneath 15 degrees slope. Furthermore, three landslides were initiated in slopes below 15 degrees slope, hence was fully excluded. Lowering the slope limit was tested in an attempt to include more landslide information, but resulted in a vast increase in crop fields being included

in the detection. In fact, throughout the “Identify” tool in ArcMap, parts of crop fields with a slope as high as 23 degrees were identified. The slope value of 23 would exclude 30 landslides and was therefore unusable in Raster Calculator.

For equation 2, removal of clouds in Raster Calculator was applied by the use of Band 2. This was only applied to Equation 2 since an earlier cloud removal process in ArcGIS Pro was done for the Sentinel 2A post-images.

The two parts of the equations that were unique, and not included in both equations, may also be the reason why Equation 2 mapped more landslides than Equation 1. The removal of crop fields excluded several landslides and parts of landslides, while the removal of clouds in Equation 2 did not affect the search for landslides.

By the use of the approach in the Raster Calculator, almost half of the landslides mapped manually were not detected. No additional landslides were mapped. Overall, with the calculation in Raster Calculator, either too much information in the context of information not concerning landslide was present in the scene, or a great amount of landslide information got lost.

7.3 Comparison to previous work by Lindsay (2021)

The background of this study introduces previous work detecting landslides in the Jølster area after the Jølster landslide event in 2019, performed by Ph.D. candidate Erin Lindsay. A comparative analysis of the differences and similarities between the method and results of this master thesis and the Ph.D. thesis by Lindsay was supposed to be accounted for. Because of limited access to the method and results of the previous study, a comparison was not possible to conduct.

7.4 Implications of this study

This study proves its importance through its contribution with new and more accurate information to the existing landslide database. In addition, it contributes to a bigger understanding of the extent and consequences after the Jølster landslide event in 2019.

Until now, only a few studies have tried combining NDVI with Sentinel 2 data to examine the NDVI potential to identify and recognize landslide change processes (Qu et al., 2021). During this study, the combination of Sentinel 2 and NDVI has proven to have a great potential in recognizing landslides. Further, the combination of Sentinel 2 and other vegetation indices such

as ARVI has also provided great results in identifying landslides. This discovery may improve landslide mapping methodology in humid regions.

8 Conclusions

This study set out to enhance the understanding of change detection analysis using optical satellite images that are post-processed to calculate various vegetation indices. More specifically, the study evaluates the applicability of satellite data produced by moderate resolution sensors and a simplified GIS workflow to provide landslide detection over large areas and regions. Four research questions were approached:

- Can optical satellite data be used to identify landslides and producing landslide inventories after heavy-rainfall events, and is this a recommended approach?
- Is moderate resolution good enough for detecting and recognize landslides?
- Does landslide size and location affect the quality of the method?
- Through a subset of six known indices, which index is most appropriate/effective to use for identifying previous landslides?

8.1 Main findings

Optical satellite data has throughout this study proven a significant contribution to detecting and recognizing landslides. 108 landslides were identified with the use of optical satellite images produced by moderate resolution sensors, vastly outperforming the previous mapping of landslides currently recorded in NVEs landslide database. In fact, 90 additional landslides to those already listed in the NVEs landslides database, after the Jølster event in 2019, were discovered. The results in this study thereby suggest the use of optical satellite data to be a recommended approach for identifying landslides and supplementing landslide inventories after heavy-rainfall events.

Further, significantly better results in the mapping and recognition of landslides were discovered with the use of Sentinel 2 data, compared to Landsat 8 data. The utilization of a 10-meter resolution allowed a more precise mapping of landslides, and is concluded to be more appropriate for the work of mapping and detecting landslides than 30-meter resolution, thus indicating to be more appropriate for mapping and detecting landslides. However, with a 30-meter resolution, Landsat 8 still contributing with recognize 30 additional landslides to those already registered, and therefore still improving the landslide inventories currently stored. Moderate resolution proved to be appropriate to use for detecting and recognizing the landslides in the tested study areas.

This study also identified big differences in the quality of the mapping between L1 and L2 data. In most cases, especially due to small-scale changes, L2 data were better at recognizing

landslides than L1 data. The size of the landslides may therefore affect the method, and the approach is recommended for detecting changes larger than 100 square meters.

From the results in this study, dARVI is concluded to be the recommended index to use for landslide detection in humid regions. Only a total of 5 landslides were mapped slightly better with dNDVI. With the use of ARVI, the location may affect the method due to finding an appropriate y-value for the specific area. Differences in atmospheric conditions affect this value.

8.2 Weaknesses

This study experienced difficulties finding an optimal Sentinel 2 post-image. Due to this, two post-images were implemented. A weakness for the manual mapping with the use of two post-images was that the mapping process became more time-consuming. To overcome this an automated cloud detection was also tried for the satellite images retrieved by the Sentinel 2 constellation. S2cloudless is a script available online, developed for Sentinel 2 images. The script was directly transferred to ArcGIS Pro where it was specified to the satellite images used in this study. This approach did not give good results, and with limited experience with python and machine learning, it was concluded not to further investigate this approach by removing clouds. Modern technology such as machine learning has the potential to supporting efficient satellite image analysis. More research should focus on automating the mapping process.

Moreover, the moderate resolution of the satellite images used in this study, made it difficult to place an exact initiating point in the manual mapping. This further affected the semi-automatic mapping of landslides in the Raster Calculator. The two equations used relied on information from the manual mapping. Without a precise initiating point, values regarding slope and elevation were inflicted. This may have excluded some potential landslides in the study area.

Another weakness due to the moderate resolution is that small-scale changes under 100 square meter were impossible to detect.

8.3 Recommendations for further work

This study found that ARVI outperformed NDVI in studying Sentinel 2 L2 data in a humid climate. Researchers should test the use of ARVI at other locations and compare ARVI and NDVI to find more explanatory factors for why and when ARVI maps better than NDVI.

Due to some of the weaknesses of this study, it would be recommended for future studies to combine optical satellite images and images taken by for example drones, with higher

resolution, for placing a more certain initiating point. Moreover, smaller landslides would also be easier to recognize with a higher resolution.

Moreover, in this study, it was not possible to compare the results and methods with previous work by Ph.D. candidate Erin. Future work should consider undertaking such comparisons as they would contribute to developing the best approach for identifying rainfall-induced landslides in humid climates. Such comparisons should identify the strengths and weaknesses of the methods used.

9 References

Aaron, J., Hungr, O., Stark, T. D., & Baghdady, A. K. (2017). Oso, Washington, landslide of March 22, 2014: dynamic analysis. *Journal of Geotechnical and Geoenvironmental Engineering*, *143*(9), 05017005.

Ackerman, S. A., Strabala, K. I., Menzel, W. P., Frey, R. A., Moeller, C. C., & Gumley, L. E. (1998). Discriminating clear sky from clouds with MODIS. *Journal of Geophysical Research: Atmospheres*, *103*(D24), 32141-32157.

Agersten, S., Andersen, A. S. H., Berger, A. C., Dyrrdal, A. V., Køltzow, M., & Tunheim, K. (2019). *Intense byger med store konsekvenser i Sogn og Fjordane 30. juli 2019* (NO. 25/2019). M. institutt.

Altaweel, M. (2017, 2017.09.07). *Methods for Creating Cloud Free Satellite Imagery: Sentinel 2*. GIS Lounge. Retrieved 2021.03.21 from https://www.gislounge.com/methods-creating-cloud-free-satellite-imagery-sentinel-2/

Andersson-Sköld, Y., Bergman, R., Johansson, M., Persson, E., & Nyberg, L. (2013). Landslide risk management—A brief overview and example from Sweden of current situation and climate change. *International Journal of Disaster Risk Reduction*, *3*, 44-61.

Bannari, A., Morin, D., Bonn, F., & Huete, A. (1995). A review of vegetation indices. *Remote sensing reviews*, *13*(1-2), 95-120.

Behling, R., Roessner, S., Golovko, D., & Kleinschmit, B. (2016). Derivation of long-term spatiotemporal landslide activity—A multi-sensor time series approach. *Remote Sensing of Environment*, *186*, 88-104.

Behling, R., Roessner, S., Kaufmann, H., & Kleinschmit, B. (2014). Automated spatiotemporal landslide mapping over large areas using rapideye time series data. *Remote Sensing*, *6*(9), 8026-8055.

Blaschke, T., Burnett, C., & Pekkarinen, A. (2004). Image segmentation methods for object-based analysis and classification. In *Remote sensing image analysis: Including the spatial domain* (pp. 211-236). Springer.

Blaschke, T., Hay, G. J., Kelly, M., Lang, S., Hofmann, P., Addink, E., Feitosa, R. Q., Van der Meer, F., Van der Werff, H., & Van Coillie, F. (2014). Geographic object-based image analysis–towards a new paradigm. *ISPRS journal of photogrammetry and remote sensing*, *87*, 180-191.

Bréon, F.-M., & Colzy, S. (1999). Cloud detection from the spaceborne POLDER instrument and validation against surface synoptic observations. *Journal of Applied Meteorology*, *38*(6), 777-785.

Burnett, C., & Blaschke, T. (2003). A multi-scale segmentation/object relationship modelling methodology for landscape analysis. *Ecological modelling*, *168*(3), 233-249.

Carrara, A., Cardinali, M., Detti, R., Guzzetti, F., Pasqui, V., & Reichenbach, P. (1991). GIS techniques and statistical models in evaluating landslide hazard. *Earth Surface Processes and Landforms*, *16*(5), 427-445.

Carrara, A., Crosta, G., & Frattini, P. (2003). Geomorphological and historical data in assessing landslide hazard. *Earth Surface Processes and Landforms: The Journal of the British Geomorphological Research Group*, *28*(10), 1125-1142.

Chang, K.-T., Chiang, S.-H., & Hsu, M.-L. (2007). Modeling typhoon-and earthquake-induced landslides in a mountainous watershed using logistic regression. *Geomorphology*, *89*(3-4), 335-347.

Cheng, K. S., Wei, C., & Chang, S. (2004). Locating landslides using multi-temporal satellite images. *Advances in Space Research*, *33*(3), 296-301.

Cruden, D. (2018). *Landslide risk assessment*. Routledge.

Deilami, K., & Hashim, M. (2011). Very high resolution optical satellites for DEM generation: A review. *European Journal of Scientific Research, 49*(4), 542-554.
Devoli, G. (2021). Personal correspondance.
Devoli, G., Colleuille, H., Sund, M., & Wasrud, J. (2020). Seven Years of Landslide Forecasting in Norway—Strengths and Limitations. Workshop on World Landslide Forum,
Devoli, G., Jarsve, K. T., Mongstad, H. H., & Sandboe, K. S. (2020). *Kontroll av registrerte skredhendelser og tildeling av kvalitetsnivå for utglidning, jordskred, flomskred og sørpeskred*. NVE. http://publikasjoner.nve.no/rapport/2020/rapport2020_31.pdf
Dorren, L. K. A. (2003). *A review of rockfall mechanics and modelling approaches* [69-87]. [London] :.
Dozier, J. (1989). Spectral signature of alpine snow cover from the Landsat Thematic Mapper. *Remote Sensing of Environment, 28*, 9-22.
DSB. (2015). *Klimahjelperen*. DSB. https://www.dsb.no/globalassets/dokumenter/veiledere-handboker-og-informasjonsmateriell/veiledere/klimahjelperen.pdf
DSB. (n.d.). *Jordskredvarsler (kartvisning)*. DSB. Retrieved 2021.03.02 from https://superset.dsb.no/superset/dashboard/Varsler-om-jordskredfare-kartvisning/#
EOS. (2019, 2019.02.22). *6 Spectral Indexes To Make Vegetation Analysis Complete*. eos. Retrieved 2021.01.30 from https://eos.com/blog/6-spectral-indexes-on-top-of-ndvi-to-make-your-vegetation-analysis-complete/
ESA. (2015). Sentinel-2 User Handbook. https://sentinel.esa.int/documents/247904/685211/Sentinel-2_User_Handbook
ESA. (n.d.-a). *Level-1*. esa. Retrieved 2021.03.27 from https://sentinel.esa.int/web/sentinel/user-guides/sentinel-2-msi/processing-levels/level-1
ESA. (n.d.-b). *Level-2*. esa. Retrieved 2021.03.27 from https://sentinels.copernicus.eu/web/sentinel/user-guides/sentinel-2-msi/processing-levels/level-2
ESA. (n.d.-c). *Overview*. esa. Retrieved 2021.04.04 from https://sentinel.esa.int/web/sentinel/missions/sentinel-2/overview
ESA. (n.d.-d). *Radiometric Resolution*. esa. Retrieved 2021.03.08 from https://sentinel.esa.int/web/sentinel/user-guides/sentinel-2-msi/resolutions/radiometric
ESA. (n.d.-e). *Sentinel-2 operations*. esa. Retrieved 2021.04.04 from https://www.esa.int/Enabling_Support/Operations/Sentinel-2_operations
ESRI. (2020). *ArcMap*. esri. Retrieved 2021.02.14 from https://desktop.arcgis.com/en/arcmap/
Fiorucci, F., Ardizzone, F., Mondini, A. C., Viero, A., & Guzzetti, F. (2019). Visual interpretation of stereoscopic NDVI satellite images to map rainfall-induced landslides. *Landslides, 16*(1), 165-174.
Fisher, P. (1997). The pixel: a snare and a delusion. *International Journal of Remote Sensing, 18*(3), 679-685.
Gómez-Chova, L., Amorós-López, J., Mateo-García, G., Muñoz-Marí, J., & Camps-Valls, G. (2017). Cloud masking and removal in remote sensing image time series. *Journal of Applied Remote Sensing, 11*(1), 015005.
Guzzetti, F., Mondini, A. C., Cardinali, M., Fiorucci, F., Santangelo, M., & Chang, K.-T. (2012). Landslide inventory maps: New tools for an old problem. *Earth-Science Reviews, 112*(1-2), 42-66.
Guzzetti, F., Reichenbach, P., Ardizzone, F., Cardinali, M., & Galli, M. (2006). Estimating the quality of landslide susceptibility models. *Geomorphology, 81*(1-2), 166-184.

Hagolle, O., Huc, M., Pascual, D. V., & Dedieu, G. (2010). A multi-temporal method for cloud detection, applied to FORMOSAT-2, VENμS, LANDSAT and SENTINEL-2 images. *Remote Sensing of Environment, 114*(8), 1747-1755.
Haugerud, R. A. (2014). *Preliminary interpretation of pre-2014 landslide deposits in the vicinity of Oso, Washington* (2331-1258).
Hay, G., Marceau, D., Dube, P., & Bouchard, A. (2001). A multiscale framework for landscape analysis: object-specific analysis and upscaling. *Landscape Ecology, 16*(6), 471-490.
Hefre, H., Gauer, P., Høydal, Ø., Sandersen, F., Kristensen, K., Breien, H., Ekseth, K., Thygeson, K. S., Gisnås, K., & Mo, K. (2019). *Faresonekartlegging i Jølster kommune* (978-82-410-1885-5). N. v.-o. energidirektorat. Norges vassdrags- og energidirektorat
Highland, L., & Bobrowsky, P. T. (2008). *The landslide handbook: a guide to understanding landslides*. US Geological Survey Reston.
Hungr, O., Evans, S. G., Bovis, M. J., & Hutchinson, J. N. (2001, Aug). A review of the classification of landslides of the flow type [Article]. *Environmental & Engineering Geoscience, 7*(3), 221-238. https://doi.org/10.2113/gseegeosci.7.3.221
Hungr, O., Leroueil, S., & Picarelli, L. (2014). The Varnes classification of landslide types, an update. *Landslides, 11*(2), 167-194.
Hunt, G. E. (1973). Radiative properties of terrestrial clouds at visible and infra-red thermal window wavelengths. *Quarterly Journal of the Royal Meteorological Society, 99*(420), 346-369.
Hölbling, D., Friedl, B., & Eisank, C. (2015). An object-based approach for semi-automated landslide change detection and attribution of changes to landslide classes in northern Taiwan. *Earth Science Informatics, 8*(2), 327-335.
Kaufman, Y. J. (1988). Atmospheric effect on spectral signature-measurements and corrections. *IEEE transactions on geoscience and remote sensing, 26*(4), 441-450.
Kaufman, Y. J., & Tanre, D. (1992). Atmospherically resistant vegetation index (ARVI) for EOS-MODIS. *IEEE transactions on geoscience and remote sensing, 30*(2), 261-270.
Klima 2050. (n.d.). *About Klima 2050*. Retrieved 2021.04.07 from http://www.klima2050.no/what-we-do
Kobayashi, N., Tani, H., Wang, X., & Sonobe, R. (2020). Crop classification using spectral indices derived from Sentinel-2A imagery. *Journal of Information and Telecommunication, 4*(1), 67-90.
Lacroix, P., Bièvre, G., Pathier, E., Kniess, U., & Jongmans, D. (2018). Use of Sentinel-2 images for the detection of precursory motions before landslide failures. *Remote Sensing of Environment, 215*, 507-516.
Lacroix, P., Zavala, B., Berthier, E., & Audin, L. (2013). Supervised method of landslide inventory using panchromatic SPOT5 images and application to the earthquake-triggered landslides of Pisco (Peru, 2007, Mw8. 0). *Remote Sensing, 5*(6), 2590-2616.
Li, Z., Shi, W., Myint, S. W., Lu, P., & Wang, Q. (2016). Semi-automated landslide inventory mapping from bitemporal aerial photographs using change detection and level set method. *Remote Sensing of Environment, 175*, 215-230.
Lindsay, E. (2017). Early warning systems for landslides triggered by hydro-meteorological processes.
Lindsay, E. (2021). Personal correspondance.
Lu, P., Qin, Y., Li, Z., Mondini, A. C., & Casagli, N. (2019). Landslide mapping from multi-sensor data through improved change detection-based Markov random field. *Remote Sensing of Environment, 231*, 111235.

Major, D., Baret, F., & Guyot, G. (1990). A ratio vegetation index adjusted for soil brightness. *International Journal of Remote Sensing, 11*(5), 727-740.
Makarau, A., Richter, R., Müller, R., & Reinartz, P. (2014). Haze detection and removal in remotely sensed multispectral imagery. *IEEE transactions on geoscience and remote sensing, 52*(9), 5895-5905.
Malamud, B. D., Turcotte, D. L., Guzzetti, F., & Reichenbach, P. (2004). Landslide inventories and their statistical properties. *Earth Surface Processes and Landforms, 29*(6), 687-711.
Martha, T. R., Kerle, N., Jetten, V., van Westen, C. J., & Kumar, K. V. (2010). Characterising spectral, spatial and morphometric properties of landslides for semi-automatic detection using object-oriented methods. *Geomorphology, 116*(1-2), 24-36.
Martha, T. R., Kerle, N., Van Westen, C. J., Jetten, V., & Kumar, K. V. (2012). Object-oriented analysis of multi-temporal panchromatic images for creation of historical landslide inventories. *ISPRS journal of photogrammetry and remote sensing, 67*, 105-119.
Matsushita, B., Yang, W., Chen, J., Onda, Y., & Qiu, G. (2007). Sensitivity of the enhanced vegetation index (EVI) and normalized difference vegetation index (NDVI) to topographic effects: a case study in high-density cypress forest. *Sensors, 7*(11), 2636-2651.
Mill, S., Ukaivbe, D., & Zhu, W. (2014). Clouds and Cloud Shadows Removal from Infrared Satellite Images in Remote Sensing System. ASEE 2014 Zone I Conference, April,
Mondini, Guzzetti, F., Reichenbach, P., Rossi, M., Cardinali, M., & Ardizzone, F. (2011). Semi-automatic recognition and mapping of rainfall induced shallow landslides using optical satellite images. *Remote Sensing of Environment, 115*(7), 1743-1757.
Mondini, A., Chang, K.-T., & Yin, H.-Y. (2011). Combining multiple change detection indices for mapping landslides triggered by typhoons. *Geomorphology, 134*(3-4), 440-451.
Mondini, A. C., Santangelo, M., Rocchetti, M., Rossetto, E., Manconi, A., & Monserrat, O. (2019). Sentinel-1 SAR amplitude imagery for rapid landslide detection. *Remote Sensing, 11*(7), 760.
NASA. (n.d.). *Landsat 8 Overview*. NASA. Retrieved 2021.04.04 from https://landsat.gsfc.nasa.gov/landsat-8/landsat-8-overview
NGU. (2014, 05.05.2021). *Skred*. ngu. Retrieved 2021.01.14 from https://www.ngu.no/emne/skred
Norsk Klimaservicesenter. (2016). *Klimaprofil Sogn og Fjordane* (Eit kunnskapsgrunnlag for klimatilpassing, Issue. N. Klimaservicesenter.
NVE. (2019, 2019.07.31). *Mye regn på kort tid ga store skader i Sogn og Fjordane 30. juli 2019*. varsom. Retrieved 2020.11.19 from https://www.varsom.no/nytt/nyheter-flom-og-jordskred/mye-regn-pa-kort-tid-ga-store-skader-i-sogn-og-fjordane-30-juli-2019/
NVE. (2020a, 2020.01.17). *Flom- og jordskredåret 2019*. Varsom. Retrieved 2021.02.08 from https://varsom.no/nytt/nyheter-flom-og-jordskred/flom-og-jordskredaret-2019/
NVE. (2020b). *Jordskred og flomskred*. nve. Norges vassdrags- og energidirektorat
NVE. (2020c, 2020.10.12). *Om skred*. nve. Retrieved 2021.01.14 from https://www.nve.no/flaum-og-skred/om-skred/?ref=mainmenu
NVE. (2021, 2021.01.28). *Flom- og jordskredåret 2020*. Varsom. Retrieved 2021.02.10 from https://www.varsom.no/nytt/nyheter-flom-og-jordskred/flom-og-jordskredaret-2020/
NVE. (n.d.). *Aktsomhetsnivåer for flom- og jordskredvarsling*. Varsom. Retrieved 2020.12.12 from https://www.varsom.no/flom-og-jordskredvarsling/aktsomhetsnivaer-for-flom-og-jordskredvarsling/

§ 29-5.Tekniske krav, (2015). https://lovdata.no/dokument/NL/lov/2008-06-27-71/KAPITTEL_4-10#%C2%A729-5
Qu, F., Qiu, H., Sun, H., & Tang, M. (2021). Post-failure landslide change detection and analysis using optical satellite Sentinel-2 images. *Landslides, 18*(1), 447-455.
Rau, J.-Y., Chen, L.-C., Liu, J.-K., & Wu, T.-H. (2007). Dynamics monitoring and disaster assessment for watershed management using time-series satellite images. *IEEE transactions on geoscience and remote sensing, 45*(6), 1641-1649.
Rossi, M., Guzzetti, F., Reichenbach, P., Mondini, A. C., & Peruccacci, S. (2010). Optimal landslide susceptibility zonation based on multiple forecasts. *Geomorphology, 114*(3), 129-142.
Roy, D. P., Wulder, M. A., Loveland, T. R., Woodcock, C. E., Allen, R. G., Anderson, M. C., Helder, D., Irons, J. R., Johnson, D. M., & Kennedy, R. (2014). Landsat-8: Science and product vision for terrestrial global change research. *Remote Sensing of Environment, 145*, 154-172.
SafeLand D4.1. (2012). Review of Techniques for Landslide Detection, Fast Characterization, Rapid Mapping and Long-Term Monitoring. https://www.ngi.no/eng/Projects/SafeLand/#Reports-and-publications
SafeLand D4.4. (2011). Guidelines for the selection of appropriate remote sensing technologies for monitoring different types of landslides. https://www.ngi.no/eng/Projects/SafeLand/#Reports-and-publications
SafeLand D4.5. (2011). *Evaluation report on innovative monitoring and remote sensing methods and future technology*. https://www.ngi.no/eng/Projects/SafeLand/#Reports-and-publications
Saunders, R. W., & Kriebel, K. T. (1988). An improved method for detecting clear sky and cloudy radiances from AVHRR data. *International Journal of Remote Sensing, 9*(1), 123-150.
Shahabi, H., Ahmad, B., & Khezri, S. (2013). Evaluation and comparison of bivariate and multivariate statistical methods for landslide susceptibility mapping (case study: Zab basin). *Arabian journal of geosciences, 6*(10), 3885-3907.
Shahabi, H., & Hashim, M. (2015). Landslide susceptibility mapping using GIS-based statistical models and Remote sensing data in tropical environment. *Scientific reports, 5*(1), 1-15.
Sharma, R. C., Hara, K., & Tateishi, R. (2017). High-resolution vegetation mapping in japan by combining sentinel-2 and landsat 8 based multi-temporal datasets through machine learning and cross-validation approach. *Land, 6*(3), 50.
Slater, P. N. (1980). Remote sensing: optics and optical systems. *Reading*.
Smith, K. (2013). *Environmental hazards : assessing risk and reducing disaster* (6th ed. ed.). Routledge.
Soeters, R., & Van Westen, C. (1996). Slope instability recognition, analysis and zonation. *Landslides: investigation and mitigation, 247*, 129-177.
Stark, T. D., Baghdady, A. K., Hungr, O., & Aaron, J. (2017). Case study: Oso, Washington, landslide of March 22, 2014—Material properties and failure mechanism. *Journal of Geotechnical and Geoenvironmental Engineering, 143*(5), 05017001.
Strout, J., & Devoli, G. (2020). Skredhendelser i Jølster i 2019: Hydro-meteorologiske forhold og skredprosesser. *Temasamling*.
Sun, Q., Zhang, L., Ding, X., Hu, J., & Liang, H. (2015). Investigation of slow-moving landslides from ALOS/PALSAR images with TCPInSAR: A case study of Oso, USA. *Remote Sensing, 7*(1), 72-88.

Tehrani, F. S., Santinelli, G., & Herrera Herrera, M. (2021). Multi-Regional landslide detection using combined unsupervised and supervised machine learning. *Geomatics, Natural Hazards and Risk, 12*(1), 1015-1038.

USGS. (n.d.-a). *Landsat 8*. usgs. Retrieved 2020.12.11 from https://www.usgs.gov/core-science-systems/nli/landsat/landsat-8?qt-science_support_page_related_con=0#qt-science_support_page_related_con

USGS. (n.d.-b). *Landsat Collection 2*. usgs. Retrieved 2021.03.27 from https://www.usgs.gov/core-science-systems/nli/landsat/landsat-collection-2?qt-science_support_page_related_con=1#qt-science_support_page_related_con

USGS. (n.d.-c). *USGS EROS Archive - Sentinel-2 - Comparison of Sentinel-2 and Landsat*. usgs. Retrieved 2020.12.08 from https://www.usgs.gov/centers/eros/science/usgs-eros-archive-sentinel-2-comparison-sentinel-2-and-landsat?qt-science_center_objects=0#qt-science_center_objects

USGS. (n.d.-d). *What is remote sensing and what is it used for?* usgs. Retrieved 2020.11.13 from https://www.usgs.gov/faqs/what-remote-sensing-and-what-it-used?qt-news_science_products=0#qt-news_science_products

Van der Meer, F., Van der Werff, H., & Van Ruitenbeek, F. (2014). Potential of ESA's Sentinel-2 for geological applications. *Remote Sensing of Environment, 148*, 124-133.

Van Westen, C. J., Castellanos, E., & Kuriakose, S. L. (2008). Spatial data for landslide susceptibility, hazard, and vulnerability assessment: An overview. *Engineering geology, 102*(3-4), 112-131.

Varnes, D. J. (1984). *Landslide hazard zonation: a review of principles and practice*.

Wartman, J., Montgomery, D. R., Anderson, S. A., Keaton, J. R., Benoît, J., dela Chapelle, J., & Gilbert, R. (2016). The 22 March 2014 Oso landslide, Washington, USA. *Geomorphology, 253*, 275-288.

Watson, K. (1994). *Airborne remote sensing for geology and the environment--present and future*. US Government Printing Office.

Yang, W., Qi, W., Wang, M., Zhang, J., & Zhang, Y. (2017). Spatial and temporal analyses of post-seismic landslide changes near the epicentre of the Wenchuan earthquake. *Geomorphology, 276*, 8-15.

Yang, W., Wang, Y., Sun, S., Wang, Y., & Ma, C. (2019). Using Sentinel-2 time series to detect slope movement before the Jinsha River landslide. *Landslides, 16*(7), 1313-1324.

Zhang, X., Wang, M., Liu, K., Xie, J., & Xu, H. (2018). Using NDVI time series to diagnose vegetation recovery after major earthquake based on dynamic time warping and lower bound distance. *Ecological indicators, 94*, 52-61.

Zhong, C., Liu, Y., Gao, P., Chen, W., Li, H., Hou, Y., Nuremanguli, T., & Ma, H. (2020). Landslide mapping with remote sensing: challenges and opportunities. *International Journal of Remote Sensing, 41*(4), 1555-1581.